Dynamic changes in mitochondria support phenotypic flexibility of microglia

Katherine Espinoza [ł,1,2], Ari W. Schaler [ł,1,2], Daniel T. Gray[1], Arielle R. Sass[1], Kamilia Moore[1], Megan E. Yu[1], Casandra G. Chamorro[1], Lindsay M. De Biase*[,1,3]

[ł] Equal contribution

* Corresponding author

[1] Department of Physiology, David Geffen School of Medicine, UCLA, Los Angeles

[2] UCLA Neuroscience Interdepartmental Graduate Program

[3] Department of Neurobiology, David Geffen School of Medicine, UCLA, Los Angeles

Correspondence should be addressed to Lindsay M. De Biase at ldebiase@mednet.ucla.edu

ABSTRACT

Microglial capacity to adapt to local tissue needs is a hallmark feature of these cells. Yet, a full understanding of the intracellular machinery that allows them to rapidly adjust their cellular phenotype is lacking. New studies show that macrophage ability to alter cellular phenotype is critically regulated by their mitochondria. Indeed, mitochondria are increasingly recognized as key intracellular signaling and regulatory hubs, in addition to their well-established role as ATP producers. Surprisingly little is known about microglial mitochondria *in vivo* and whether they play similar roles in regulating microglial capacity to alter cellular phenotype. Here, we generated novel transgenic crosses for accurate visualization of microglial mitochondria and found, unexpectedly, that mitochondria did not appear to regulate microglial tissue surveillance. However, brain regions where microglia show early responses to aging also showed early changes in microglial mitochondria. Microglial mitochondria were also altered within hours of LPS injections and microglial expression of inflammation-, trophic-, and phagocytosis-relevant genes was strongly correlated with expression levels of specific mitochondria-relevant genes. Finally, direct genetic manipulation of microglial mitochondria altered microglial morphology and led to brain-region specific effects on microglial gene expression. Overall, this study provides foundational information about microglial mitochondria and their relationship to differences in cell phenotype that occur across brain region, during pathological insults, and during aging.

INTRODUCTION

An essential and defining characteristic of microglia is their ability to rapidly remodel their attributes and shift into different functional states[1–3]. In different brain regions, microglia adapt to local tissue needs and exhibit prominent regional differences in cell density, morphology, motility, and phagocytic behaviors[4–9]. They also alter numerous cell attributes and adopt distinct phenotypes as they respond to chronic stress, high fat diet, pollution exposure, aging, brain injury, and disease[10–16]. Microglial capacity to shift into a range of functional states in response to these varied CNS challenges can potently impact neuronal health.

To sense the status and needs of the local environment, microglia express an impressive repertoire of cell surface receptors[17–19]. Microglia also continually extend and retract their cell processes into the surrounding tissue[20–22], contacting nearby cells and other structures. The field has elucidated how cell surface receptors such as P2RY12, TLR4, TGFBR2, CX3CR1, CR3 (ITGAM), and CSFR1 provide microglia with information about their environment and regulate changes in cell properties and functions. Yet, there are major gaps in our understanding of how microglia “interpret” simultaneous streams of information coming from all these signaling axes and convert this into well-orchestrated remodeling of cell attributes to achieve the needed cellular phenotype.

Recent findings suggest that mitochondria may play an essential role in regulating changes in cell attributes. Classically thought of as the ATP producing “powerhouse” of the cell, mitochondria are now recognized as critical signaling hubs[23–26]. Mitochondria influence intracellular signaling by buffering calcium, by providing metabolites needed for protein post-translational modifications, by interacting physically with other organelles, and by signaling to the nucleus to impact gene expression[23–26]. Research in macrophages supports this view of mitochondria as signaling hubs, demonstrating that mitochondria regulate macrophage responses to pathology and shifts into distinct inflammatory states[27–33]. Key observations suggest a similarly important role for these organelles in regulating changes in microglial cellular

phenotype. Regional differences in microglial phenotype are accompanied by prominent differences in expression of mitochondrial-relevant genes[34], and the state of mitochondria appears to be linked to microglial responses to early life immune challenge, brain injury, and protein aggregates in neurodegenerative disease[35–38]. Yet, direct and rigorous study of these organelles in microglia *in vivo* is minimal and large gaps persist in our knowledge about potential mitochondrial regulation of microglial attributes. In this study, we use novel transgenic crosses and multidisciplinary approaches to define for the first time the mitochondrial landscape within microglia *in vivo* and explore the relationship of these organelles to microglial phenotypic remodeling across brain regions, in response to inflammatory insult, and during aging.

RESULTS

Region-specific phenotypes of microglia are accompanied by regional differences in mitochondrial mass and number.

Mitochondrial abundance, morphology, and molecular composition vary dramatically across cell types[39], arguing that findings about how these organelles impact cellular function cannot be generalized across cell types. Yet study of mitochondria *in vivo* is challenging, in part, because it is difficult to clearly identify mitochondria of specific cell types with immunostaining approaches, which label all mitochondria in all cells within the tissue. For clear visualization of microglial mitochondria *in vivo*, we crossed mice that express inducible cre recombinase in microglia (*CX3CR1*$^{CreER/+}$) with mice that express Cre-dependent mitochondrial-targeted GFP (*mitoGFP*) (**Fig. 1A**) [40,41]. In fixed tissue from young adult (2mo) double transgenic *CX3CR1*$^{CreER/+}$*;mitoGFP* mice (*MG-mitoGFP* mice hereafter), numerous GFP+ structures could be observed throughout the somas and cell processes of microglia (**Fig. 1B** and **Fig. S1A,B**). Consistent with reports of tamoxifen-independent recombination when using *CX3CR1*$^{CreER/+}$ and reporters with minimal distance between loxP sites[42,43], significant recombination was observed in *MG-mitoGFP* mice without tamoxifen administration. In fixed tissue from nucleus accumbens (NAc) and ventral tegmental area (VTA), two brain regions where microglia display distinct cellular phenotypes, roughly 60-85% of IBA1+ microglia contained GFP-tagged mitochondria (**Fig. S1A - C**). Flow cytometry in midbrain (containing VTA) and striatum (containing NAc), similarly indicated that approximately 80% of microglia were GFP+ in the absence of tamoxifen injection (**Fig. S1D- F**) and GFP was not observed in other CNS cells (**Fig. S1G**). Finally, in acute brain sections from *MG-mitoGFP* mice, GFP+ structures were consistently colocalized with tetramethylrhodamine (TMRM), a mitochondrial membrane potential indicator, confirming that GFP-tagged structures are mitochondria (**Fig. S1H-I**). Together these results indicate that *MG-mitoGFP* mice accurately reveal the *in vivo* distribution of microglial mitochondria.

To explore the relationship between mitochondrial networks and baseline structure of microglia in young adult mice, we carried out high resolution confocal imaging and 3D reconstruction of both microglia and their mitochondria in the NAc and VTA (**Fig. 1B** and **Fig. S2A**), where microglia show prominent differences in cell density, branching complexity, and gene expression[34]. Consistent with previous findings, microglial tissue coverage in the VTA was lower than that observed in NAc[34] (**Fig. 1C**). 3D reconstruction of microglial mitochondria revealed that volume of individual mitochondria ranged from 1-40 μm^3, and average mitochondrial sphericity, aspect ratio (measure of elongation), and max volume were relatively consistent across NAc and VTA microglia (**Fig. S2B-D**). However, despite showing reduced tissue coverage, VTA microglia exhibited a greater number of mitochondria relative to cell volume, as well as a greater total mitochondrial volume relative to cell volume (mitochondrial mass) (**Fig.**

1D, E). Together, these observations indicate that regional differences in microglial cellular phenotype are accompanied by regional differences in mitochondrial metrics.

Mitochondrial number is correlated with morphological complexity of microglia, particularly in the VTA.

Microglial capacity to survey the surrounding brain tissue is influenced by cell branching and morphological complexity. To explore how mitochondrial networks relate to microglial branching structure, we crossed *MG-mitoGFP* mice to Ai14 reporter mice to drive cytosolic expression of TdTomato (TdTom) along with GFP tagging of microglial mitochondria (**Fig. 1A** and **Fig. S2E**)[40,41,44]. In the absence of tamoxifen injection, incidence of mitoGFP+TdTom+ cells was low enough to allow rigorous and unequivocal reconstruction of the branching patterns of individual microglial cells, as well as their mitochondrial networks (**Fig. 1F**). Consistent with previous findings[34], VTA microglia exhibited lower morphological complexity than NAc microglia in young adult *MG-mitoGFP;Ai14* mice (**Fig. 1G-I**).

In comparing morphological and mitochondrial features of microglia, Sholl analysis revealed that both cell process branching, and number of mitochondria reached a maximum at 20-25 μm from the cell soma in both the NAc and the VTA (**Fig. S2F-G**). As might be expected total cell process length was correlated with total volume of mitochondria in NAc microglia (**Fig. 1L**, and **Fig. S2I**), suggesting that a greater mass of mitochondria are generated to support a greater mass of cell processes. Somewhat surprisingly, both total number of branch points and maximum number of Sholl intersections were positively correlated with total mitochondrial number in VTA microglia. Hence, for VTA microglia, the architecture of cell processes, rather than simply the total amount of cell processes, was related to mitochondrial number (**Fig. 1J, K,L**). Together these analyses suggest that baseline microglial and mitochondrial morphology are interlinked and that changes in microglial morphology are likely accompanied by remodeling of mitochondrial networks within these cells.

Mitochondrial number and mitochondrial motility are not aligned with microglial tissue surveillance.

Continual morphological remodeling of microglia as they survey the surrounding tissue is assumed to be an energy intensive process. However, the relationship between microglial cell process motility and mitochondrial abundance has not been explored. We performed two-photon imaging in acute brain sections prepared from young adult (2-3mo) *MG-mitoGFP;Ai14 mice* and recorded motility of both microglial cell processes (TdTom) and mitochondria within these cells (GFP) (**Fig. 2** and **Fig. S3**). Microglia were imaged at least 60μm below the surface of the brain section and microglial motility (total process remodeling, normalized to cell area) was not correlated with time elapsed since preparation of brain sections (**Fig. 2D**) or number of Sholl intersections (**Fig. S3E**), suggesting that observed dynamics are not primarily driven by responses to brain slice preparation. Finally, similar to observations in fixed tissue, total mitochondrial volume and microglial Sholl intersections were positively correlated (**Fig. S3D**), indicating that this preparation is well suited for initial exploration of relationships between mitochondria and microglial cell dynamics.

Microglial motility was similar across NAc and VTA microglia (**Fig. 2C**), implying that less of the surrounding tissue is surveyed during a given interval in the VTA, as VTA microglia are less branched and have lower tissue coverage compared to NAc microglia (**Fig. 1C, G-I**). Although VTA microglia showed greater mitochondrial mass compared to NAc microglia (**Fig. 1D**), there

was no correlation between total mitochondrial volume and microglial motility in the VTA (**Fig. 2E**). In the NAc, there was a negative correlation, such that microglia with lower total mitochondrial volume showed greater cell process motility (**Fig. 2E**). These observations suggest that there is a more robust relationship between mitochondrial abundance and underlying cell morphology than with dynamic remodeling of that morphology.

Microglial mitochondria themselves also exhibited motility that included "jitter," concerted directional movement, and occasional examples of fission and fusion (**Fig. 2F-H**). 3D reconstruction of mitochondria in Imaris and tracking across time revealed that mitochondrial motility (total displacement over time) was similar in NAc and VTA microglia (**Fig. 2I**). Linear regression analyses indicated that there was no significant relationship between average mitochondrial displacement and cell process remodeling of microglia in either the NAc or the VTA **(Fig. 2J)**. This finding further reinforces the idea that mitochondria are not linked in any direct fashion to baseline microglial tissue surveillance.

Mitochondrial distribution is stable during early phases of microglial response to focal injury.

In addition to homeostatic tissue surveillance, microglia exhibit rapid and robust cell process extension toward focal sites of CNS injury[20,45]. We also imaged microglial processes and mitochondria before and after focal laser lesions and, consistent with previous findings in the field[46,47], found that microglia rapidly extended cell processes and contacted the lesion within 10-15min (**Fig. 3A-F**). Surprisingly, these rapidly extending cell processes did not contain any mitochondria and no mitochondria were trafficked into lesion-responsive cell processes even 70min post-lesion (*not shown*). Moreover, there did not appear to be obvious changes in somatic mitochondria or redistribution of mitochondria in processes on the non-lesion side of the cell. Future experiments using *in vivo* imaging will be needed to explore whether changes in mitochondrial distribution within injury responsive microglia emerge several hours post-lesion.

Mitochondrial remodeling is evident at the earliest stages of microglial responses to inflammatory challenge.

To further explore the role of mitochondria in microglial responses to pathological challenges, we used intraperitoneal (i.p.) injections of lipopolysaccharide (LPS), a component of the cell wall of gram-negative bacteria, to model inflammatory responses that accompany infection. Microglia show prominent changes in gene expression within hours of LPS injection and changes in morphology by 24-48 hours post-injection[48]. *In vitro* LPS exposure alters microglial mitochondrial structure and function[49–52] and, in macrophages, mitochondrial alterations play an essential role in enabling and regulating changes in macrophage attributes as they respond to inflammatory challenges[28–33,53,54].

Young adult (3-4mo) *MG-MitoEGFP* mice were given i.p. injections of saline or LPS and microglial gene- and protein- expression were analyzed via FACS and downstream qPCR (**Fig. 4A**). Within 4hr of LPS challenge, microglia from both striatum (STR, containing NAc) and midbrain (MB, containing VTA) upregulated transcripts for pro-inflammatory factors (*Il1β, Tnfα*), and downregulated transcripts for homeostatic microglial genes (*Tgfβ1, P2ry12, Cx3cr1*), consistent with previous studies[48,55]. Upregulation of genes associated with microglial phagocytic function (*Cd45, Itgam*) was evident by 24hr post injection (**Fig. 4B** and **Table S1,**

S2). Overall, STR and MB microglia responded similarly to LPS challenge at the gene expression level.

Microglial expression of mitochondrial-function related genes was also altered at both 4hr and 24hr post injection (**Fig. 4B** and **Table S1, S2**). Within 4hr of LPS challenge, genes related to mitochondrial ROS handling (*Sod2, Cat*), mitochondrial fission (*Dnm1l*), and mitochondrial biogenesis (*Nrf1*) were significantly altered. Some of these gene expression changes were maintained into 24hr post injection (*Sod2, Dnm1l*), while others appeared more restricted to the 4hr time point (*Cat, Nrf1*). At 24hr post injection, prominent upregulation of electron transport chain component genes *Ndufa12* (Complex I), *Cox4i1* (Complex IV), and *Atp5d* (Complex V) emerged. Genes related to mitochondrial calcium handling (*Vdac1, Micu1*) were also significantly altered. Again, most gene expression changes were similar across STR and MB, (**Fig. 4B** and **Table S1, S2**).

To further probe the relationship between mitochondrial state and key features of microglia as they respond to inflammatory challenge, we used Principal Component Analysis (PCA) and found that PCA based solely on expression patterns of mitochondrial function-relevant genes can explain 64.7% of sample variation with the first 2 components and 81% of variation with the first 3 components (**Fig. S4A**). Moreover, 24hr post injection samples cluster away from Saline samples (**Fig. 4C**) and 4hr post injection samples are interspersed among Saline samples or skewed toward the 24hr samples. Hence, without even considering microglial inflammatory genes or homeostatic genes, microglia that are responding to LPS challenge can be clearly identified on the basis of their mitochondrial function profiles. We also used linear regression analyses and found numerous correlations between individual microglial-state and mitochondrial state genes (**Fig. 4D** and **Table S3**). For example, expression of homeostatic microglial genes *Cx3cr1* and *P2ry12* showed significant correlation with electron transport chain genes (*Cox4i1, Ndufa12, Sdha*) and mitochondrial biogenesis genes (*Nrf1, Tfam, Ppargc1a*) in saline treated animals but the majority of these correlations were lost at 4hr post LPS. Microglial pro-inflammatory genes *Il1β* and *Tnfα* showed significant correlation with mitochondrial biogenesis genes (*Nrf1, Tfam*), mitochondrial fusion and fission genes (*Mnf1, Dnm1l*) and the ROS handling gene *Sod2* at 4hr post LPS (**Fig. 4D** and **Table S3**). Microglial- and mitochondrial-gene correlations remained abundant and continued to evolve at 24hrs post LPS.

Together these data indicate that numerous facets of mitochondrial function are remodeled during microglial responses to inflammatory challenge and that mitochondrial remodeling begins at the earliest stages of microglial responses to inflammatory challenge. Moreover, *Cd68*, a key microglial lysosome gene, did not show significant correlations with expression of microglial pro-inflammatory factors *Tnfα* and *Il1β* and few *Cd68* correlations with other genes were modulated by LPS treatment (**Fig. S4B** and **Table S4**), providing initial hints that mitochondria, as organelles, may have a unique ability to regulate microglial functional state during inflammatory challenge.

The qPCR-based analyses presented thus far show high sensitivity for detection of early changes in cell and organelle state following LPS challenge. However, not all transcript level changes are maintained at the protein level. We also analyzed data recorded during FACS isolation of microglia and found that the intensity of GFP, reflecting mitochondrial mass, showed significant increases at 24hr post injection in both the STR and MB, with hints of emerging increases at 4hrs post injection (**Fig. 4E, 4F**). In contrast, mitochondrial membrane potential, as detected by TMRM intensity, decreased significantly at 24hr post LPS (**Fig. 4E, 4F**). These

changes in mitochondrial mass and mitochondrial membrane potential were accompanied by significant protein-level increases in CD45 by 24hr in STR microglia and trends toward increased CD45 in MB microglia. Protein level expression of CX3CR1 and P2RY12 differed across region but not across treatment (**Fig S4C**). These data confirm that changes in mitochondrial state at the protein and functional level are associated with changes in microglial protein-level expression.

Increased mitochondrial mass and mitochondrial elongation are associated with microglial responses to inflammatory challenge.

To investigate how LPS challenge impacts morphology of microglial mitochondria, we analyzed fixed tissue from 3-4mo *MG-MitoEGFP* mice (**Fig. 5A**, **Fig. S5A**) at 24hr post-LPS, when protein-level changes in microglia and their mitochondria were most evident via FACS (**Fig. 4**). 3D reconstruction of both microglia and their mitochondria in NAc and VTA revealed significant increases in mitochondrial mass at 24hr post LPS (**Fig. 5B**), consistent with FACS-based analyses of GFP and qPCR-based increases in mitochondrial biogenesis factors *Nrf1* and *Tfam*. No significant changes in mitochondrial number were detected (**Fig. 5C**) and, instead, microglial mitochondria showed significant elongation, as detected by increases in aspect ratio, a measure of the mitochondria's longest axis divided by its shortest axis (**Fig. 5D**). Elongation of mitochondria has been associated with increased capacity for oxidative phosphorylation[56,57], which would be consistent with the qPCR-based observation of robust increases in electron transport chain components (*Ndufa12, Atp5d, Cox4i1, Sdha*) at 24hrs post LPS (**Fig. 4B**). Collectively, these findings indicate that microglial mitochondria also undergo structural remodeling as microglia respond to inflammatory challenge.

Microglial mitochondria undergo morphological and functional changes during aging.

Microglia exhibit numerous changes during aging, including altered morphology and inflammatory profile[12,58–60]. Results described above indicate that there are key relationships between mitochondria and microglial morphology (**Fig. 1**) as well as microglial inflammatory profile (**Fig. 4**). We analyzed NAc and VTA microglial mitochondria in fixed tissue from middle age (12-13mo) and late middle age (16-18mo) *MG-MitoEGFP* mice (**Fig. 6A**) and compared them to microglial mitochondria in young adult (2-3mo) mice. With age, mitochondrial mass tended to increase, particularly in the VTA and significant increases in mitochondrial number were observed in both NAc and VTA microglia (**Fig. 6B,C**). VTA microglia also showed significant increases in mitochondrial elongation at 16-18mo (**Fig. 6B,C**). Within mouse comparisons using paired t-tests revealed that the elevated mitochondrial mass and mitochondrial number in VTA microglia relative to NAc microglia that were observed at 2-3mo were no longer significant at 12-13mo and 16-18mo, likely due to increased mouse to mouse variation (**Fig. S6A,B**). Finally, an elevated aspect ratio (greater mitochondrial elongation) was evident in VTA relative to NAc microglia at 16-18mo (**Fig. S6C**). These findings indicate that microglial mitochondria undergo multiple age-related structural changes with both similarities and differences in these changes across brain region.

FACS-based analysis of microglia from 3mo and 18mo *MG-mitoEGFP* mice revealed that intensity of GFP was significantly increased with age in both STR (containing NAc) and MB (containing VTA) microglia (**Fig. S6D**), pointing to increases in mitochondrial mass. Conversely, mitochondrial membrane potential (TMRM intensity) was significantly reduced with age in both regions (**Fig. 6D,E**). To elucidate age-related functional differences even further, we analyzed

TMRM intensity of microglia in WT mice and included an intermediate 12-13mo timepoint. In this analysis, MB microglia exhibited slightly more depolarized mitochondrial membrane potential (lower TMRM intensity) than STR microglia in 2-3mo old mice (**Fig. 6F**). These regional differences grew larger in 12-13mo old mice and even larger in 16 18mo old mice. Across ages, both regions showed significant changes in mitochondrial membrane potential, with MB microglia showing significant depolarization in 12-13mo and 16-18mo mice compared to 2-3mo mice. Interestingly, STR microglia exhibited hyperpolarized mitochondrial membrane potential (higher TMRM intensity) in 12-13mo mice compared to 2-3mo mice. At 16-18mo, however, they showed depolarized mitochondrial membrane potential, similar to MB (**Fig. 6F**). Together, these findings indicate that the functional status of microglial mitochondria changes significantly during aging, with key differences across brain region. Moreover, they suggest that remodeling of mitochondrial status begins in middle age, which aligns with the period when VTA microglia begin to show key aging features[61].

Targeted genetic manipulation of microglial mitochondria elicits changes in mitochondrial morphology and gene expression.

To further probe how mitochondrial state may regulate microglial phenotype, we crossed *CX3CR1*$^{CreER/+}$ mice with *Tfam*$^{fl/fl}$ mice to achieve targeted deletion of mitochondrial transcription factor A (TFAM) in microglia (*MG-TFAMKO* or *MG-mitoGFP-TFAMKO*)(**Fig. 7A**). TFAM deletion in diverse cell types leads to reduced expression of electron transport chain subunits encoded by mitochondrial DNA, as well as changes in mitochondrial membrane potential and mitochondrial morphology[62,63]. For all experiments, mice were injected with 4-hydroxytamoxifen and analyzed 2 months later to allow for both TFAM deletion and turnover of existing mitochondrial components that will be impacted by TFAM deletion as mitochondrial proteins are among the most long lived[64]. qPCR from FACS isolated MB and STR microglia confirmed downregulation of *Tfam* in *MG-TFAMKO* mice relative to controls (**Fig. 7B**). Analysis of both mitochondria and microglia via histology in *MG-mitoGFP-TFAMKO* mice and controls revealed that mitochondrial volume, number and sphericity increase following TFAM loss (**Fig. 7C-F, Fig.S7A**). To determine how these genetically induced changes in mitochondrial status relate to microglial properties, we also analyzed microglial volume. There were no significant differences in mitochondrial mass or normalized mitochondrial number in control versus *MG-mitoGFP-TFAMKO* mice (**Fig. 7G-H**). However, microglial tissue coverage was significantly increased in both NAc and VTA microglia following TFAM loss (**Fig. 7I**). These findings demonstrate tight links between mitochondrial state and microglial morphology.

Qualitatively, loss of TFAM appeared to increase GFP intensity of mitochondria in *MG-mitoGFP-TFAMKO* mice. We investigated this by quantifying mean and max GFP intensity in mitochondria across NAc and VTA and found increases in both compared to controls (**Fig. 7J, S7B-C**). Also qualitatively, it appeared that some microglia in *MG-mitoGFP-TFAMKO* mice exhibited more prominent changes in mitochondrial morphology and GFP brightness compared to others **(Fig. 7C and Fig. S7A)**. To further probe this apparent cell-to-cell variation, we analyzed individual microglia from NAc and VTA and, indeed, observed increased variability in the mitochondrial sphericity and number from individual cells in *MG-mitoGFP-TFAMKO* mice compared to controls (**Fig. S7D,E**). The cell-to-cell variation likely reflects that Cre-induced recombination and removal of TFAM is not occurring in 100% of microglia.

As another approach to explore how genetically targeted manipulation of microglial mitochondria affects microglial properties, we FACS-isolated STR and MB microglia and analyzed expression of a panel of microglial- and mitochondrial-function related genes via qPCR. PCA analysis revealed that *MG-TFAMKO* samples from STR and MB appeared to

cluster separately (**Fig. 8A** and **Fig. S8A**), suggesting that TFAM loss exerts distinct effects on STR and MB microglia. Further investigation of fold changes for individual genes revealed that TFAM knockout indeed induced a variety of changes in both mitochondrial and microglial genes that occurred in a region-specific manner (**Fig. 8B**, **8C, Fig. S8B** and **Table S5**). *Cox4i1* and *Atp5d* (genes related to the electron transport chain) exhibited significant increases in MB but not STR microglia of *MG-TFAMKO* mice compared to control. Genes related to mitochondrial ROS handling, *Sod2* (**Fig. 8B**) and *Cat* (**Fig. S8B**), and mitochondrial calcium handling, *Micu1*and *Vdac1* (**Fig. S8B**), exhibited significant decreases in *MG-TFAMKO* STR microglia compared to control, but were not significantly altered in MB microglia.

These changes in mitochondrial state upon TFAM knockout were accompanied by significant changes in genes related to key microglial functions. Similar to observations from mitochondrial genes, many of the changes in microglial function genes were also region specific. Proinflammatory transcripts *Il1β* and *Tnfα* were significantly increased in MB microglia while significant decreases in *Tgfβ1* and *Cx3cr1* were observed only in STR microglia (**Fig. 8C**). Genes involved in microglial phagocytic pathways (*Cd45* and *Cd68*) were also found to be significantly decreased in *MG-TFAMKO* STR microglia (**Fig. 8C**). Collectively, these data indicate that mitochondrial state and microglial functional state are tightly intertwined and highlight the potential for important regional differences in this interrelationship.

DISCUSSION

Mitochondrial dysfunction has been associated with developmental delays, epilepsy, psychiatric disorders, aging, and neurodegeneration[65,66]. A key priority in uncovering how mitochondria become disrupted in these contexts is understanding how mitochondria impact the function of specific CNS cells. However, because mitochondrial structure and molecular composition vary widely across distinct cell types[39], findings about the functional roles of these organelles cannot be generalized and mitochondria need to be studied with cellular specificity. Our study is one of the first to provide detailed information about microglial mitochondria *in vivo* and supports the idea that mitochondrial function is distinct across CNS cells. We observed that mitochondria occupy about 4-6% of microglial volume, and entire microglial branches sometimes have few, if any, mitochondria (**Fig. 1** and **Fig. 2**). This is similar to mature oligodendrocytes, where mitochondria make up about 4% of cell volume[67] but unlike astrocytes where mitochondria make up about 80% of astrocyte volume in young adult mice[68]. Qualitatively, our experiments using TMRM incubation in acute brain sections also suggest that microglial mitochondria are less hyperpolarized than mitochondria of surrounding cells (**Fig. S1H**).

Previous studies have suggested that mitochondrial function in microglia changes in the context of disease, stress, and immune activation[35,36,47,49,69]. Almost nothing is known, however, about how these organelles are linked to physiological functions of microglia. We found key relationships between mitochondrial abundance and total process length as well as branching complexity of microglia (**Fig. 1**). Hence, even if microglia have fewer mitochondria than other CNS cells, our data suggest that these organelles play a key role in shaping general cellular architecture of microglia. Our qPCR-based analyses also indicated that expression of homeostatic microglial genes such as *P2ry12*, *Cx3cr1*, and *Tgfβ1* was significantly correlated with expression of multiple mitochondrial genes, suggesting further relationships between these organelles and basal cellular phenotype. Regional specialization is also a key feature of homeostatic microglia[4,8,9,34,70] and we found that regional differences in microglial cellular phenotype were accompanied by regional differences in mitochondrial mass, mitochondrial number, and mitochondrial membrane potential in young adult mice (**Fig. 1** and **Fig. 6**).

Together, these observations indicate that mitochondrial status is tightly linked to key microglial attributes under physiological conditions.

One of the most surprising findings of our study, however, involved microglial tissue surveillance, a hallmark physiological function of these cells[20,21]. We found that microglial cell process motility did not show a positive correlation with abundance of mitochondria (**Fig. 2**). We also analyzed movement of the mitochondria themselves and observed the same forms of dynamic mitochondrial remodeling described in other cell types. Yet, we failed to find any association between mitochondrial displacement and cell process motility, suggesting that mitochondrial trafficking to specific subcellular locations is not required for baseline microglial tissue surveillance. Finally, we found that mitochondria are relatively stable within microglia as they rapidly extend cell processes toward focal laser lesions (**Fig. 3**). Microglial tissue surveillance and rapid tissue injury responses are assumed to be energy intensive processes. Future studies will need to investigate highly localized relationships between microglial filopodia and nearby mitochondria to examine whether mitochondrial membrane potential or other features of mitochondrial state (e.g. fission and fusion) are linked to movement of adjacent cell processes.

We also examined microglial responses to systemically injected LPS, which evolve over a longer time course (hours to days) than microglial responses to laser lesion[48]. We found that early increases in microglial *Tnfα* and *Il1β* mRNA were accompanied by altered expression of multiple mitochondrial-relevant genes (**Fig. 4**). Moreover, expression levels of *Tnfα*, *Il1β*, and *Cd45* in individual samples at 4hr post-LPS were significantly correlated with expression levels of genes involved in mitochondrial fission and fusion, calcium handling, and ROS handling, in addition to genes involved in mitochondrial biogenesis and oxidative phosphorylation. These findings support the possibility that mitochondrial signaling *regulates* changes in microglial attributes rather than a simply altering energy production to support a newly emerging cellular phenotype.

Indeed, the mitochondrial field has moved well beyond viewing this organelle solely as an energy producer, and additionally supports a model in which mitochondria act as critical signaling and regulatory centers within the cell. Consistent with this model, using targeted deletion of TFAM, we showed that using genetic approaches to alter microglial mitochondrial status led to changes in microglial and mitochondrial morphology and gene expression (**Fig. 7** and **Fig. 8**). Importantly, the impact of TFAM deletion on microglial cellular phenotype varied across brain regions. VTA/MB microglia showed upregulation of proinflammatory genes and a unique pattern of altered mitochondrial-relevant genes compared to microglia in NAc/striatum. This mirrors our findings in the context of aging, which is known to alter mitochondrial state. Previously, we had shown that VTA microglia exhibit early increases in proliferation and production of inflammatory factors during aging[61] and here we demonstrated VTA/MB microglia also show earlier aging-induced alterations in their mitochondria (**Fig. 6**). Multiple mutations that increase risk for neurodegenerative disease are in mitochondrial-relevant genes[23,71,72]. Altogether, our findings support the idea that VTA/MB microglia are uniquely vulnerable to perturbations of mitochondrial function and that this may shape which populations of nearby neurons are most vulnerable to aging-associated neurodegenerative disease.

Mitochondria are highly complex organelles and much remains to be elucidated about how specific facets of mitochondrial state impact specific microglial attributes and functions. Our study provides foundational insight into how these organelles align with key physiological

properties of microglia as well as their attributes during responses to CNS insults. These findings highlight that further study of mitochondrial state and how it regulates microglial cell phenotypes should be a priority for the field.

MATERIALS AND METHODS

Mouse lines.

C57Bl6 WT mice were obtained from the NIA Aged Rodent Colony and housed in the UCLA vivarium for at least one month before experiments. *CX3CR1* $^{CreER/+}$ mice were originally obtained from Jackson Labs (stock #025524) and subsequently maintained in our colony [73]. *Rosa26-lsl-mito-EGFP* mice (*mitoEGFP* mice) were obtained from Dr. Jeremy Nathans (Johns Hopkins University) and are available at Jackson Labs (stock #021429). These mice enable cre-dependent expression of GFP that is fused to an N-terminal signal derived from mouse cytochrome c oxidase, subunit VIIIa, enabling specific localization to mitochondria [74]. Ai14 td tomato reporter mice were obtained from Jackson Labs (stock #007914) and subsequently maintained in our colony [75]. Mice used for experiments were heterozygous for these transgenes. *Tfam*$^{fl/fl}$ floxed mice were obtained from Jackson Laboratories where *loxP* sites flank exons 6-7 of the transcription factor A, mitochondrial (*Tfam*) gene (stock #026123, cite https://pubmed.ncbi.nlm.nih.gov/9500544/). These mice were crossed to the *CX3CR1*^{CreER} *mice resulting in deletion of exons 6-7 in microglia. Tfam*$^{fl/fl}$ were homozygous. In all experiments balanced numbers of male and female mice were used. Mice were housed in normal light/dark cycle and had ad libitum access to food and water. All experiments were performed in strict accordance with protocols approved by the Animal Care and Use Committees at UCLA.

Lipopolysaccharide Injections.

CX3CR1 $^{CreER/+}$*; mitoEGP mice* 3 to 5 months of age (mos) received single intraperitoneal injections of 1mg/kg of Lipopolysaccharide (LPS) (Millipore Sigma, strain O55:B5, L2880-25MG) or saline. All injections were performed around ~10am and mice were euthanized for immunohistochemistry or flow cytometry at 4 h or 24 h post-injection.

Tamoxifen Injections.

CX3CR1$^{CreER/+}$*; mitoEGP*$^{EGFP/+}$*; TFAM*$^{Fl/Fl}$ mice and *CX3CR1*$^{CreER/+}$*;TFAM*$^{Fl/Fl}$ at 3-4 mos received injections of 4-Hydroxytamoxifen twice a day for 3 days at 1mg/kg. The mice were housed for 2 months after injections before euthanized for immunohistochemistry or flow cytometry.

Tissue collection and immunohistochemistry.

CX3CR1 $^{CreER/+}$*; mitoEGFP* (postnatal day 60, 12-13mo, and 16-18mo), *CX3CR1* $^{CreER/+}$*; mitoEGFP ; Ai14* (postnatal day 60) or *CX3CR1*$^{CreER/+}$*; mitoEGP*$^{EGFP/+}$*; TFAM*$^{Fl/Fl}$ (6-7mos) mice were deeply anesthetized via isoflurane inhalation and transcardially perfused with 1M phosphate buffered saline (PBS; pH 7.4) followed by ice-cold 4%

paraformaldehyde (PFA) in 1M PBS. Brain tissue was isolated and postfixed PFS for ~4h at 4°C and then stored in 1 M PBS with 0.1% sodium azide until sectioning. Coronal brain sections were prepared using a vibratome at 60 mm thickness. For immunostaining, free-floating brain sections were washed with 1M PBS (5 min) and then permeabilized and blocked in a solution of 2% bovine serum albumin (BSA) and 3% normal donkey serum (NDS) and 0.01% of Triton-X for 2 h with rotation at room temperature. Sections were then incubated overnight with primary antibodies prepared in 2% bovine serum albumin (BSA) and 3% normal donkey serum (NDS) at 4°C with rotation. Sections from aged mice were incubated in TrueBlack lipofuscin autofluorescence quencher, (5%; Biotium cat: 23007) for 60 s followed by a 3x5 min rinse in 1M PBS prior to incubation with primary antibodies. Following primary antibody incubation, sections were washed 3x with 1M PBS and then incubated with secondary antibodies prepared in 2% bovine serum albumin (BSA) and 3% normal donkey serum (NDS) at room temperature for 2 h with rotation. This was followed by washes in 1M PBS (3x) with second wash containing 1:4000 dilution of DAPI in 1 M PBS. Sections were mounted using Aqua-Poly/Mount (Polysciences cat: 18606) and cover slipped (coverslips of #1.5 thickness). Primary antibodies used include rabbit anti- Iba1 (1:800; Wako, catalog #019-19741), rat anti-CD68 (1:200; clone FA11, AbD Serotec, catalog #MCA1957), chicken anti-TH (1:500; Aves, catalog #TYH). Secondary antibody combinations include rabbit AlexaFluor-647, chicken AlexaFluor-594, rat AlexaFluor-594, or chicken AlexaFluor-405 (used at 1:1000; all raised in donkey; Jackson ImmunoResearch Laboratories). For each set of analyses, three brain sections containing nucleus accumbens (NAc) and three brain sections containing ventral tegmental area (VTA) were chosen from each mouse. Brain sections were selected based on well-defined anatomical parameters and were matched for anterior-posterior location.

Confocal image acquisition and analysis.

Fixed tissue slides were imaged using a Zeiss LSM880 confocal microscope or a Zeiss LSM700 confocal microscope. Within the NAc, images were acquired at the boundary between core and shell (identified anatomically) and include both subregions. In the VTA, images captured were medial to the medial lemniscus. For quantification of MitoEGFP recombination within microglia, stacks of confocal images (z stacks) with a z interval of 1 μm were taken using a 20x objective and imported into ImageJ software for analysis. Maximum intensity projections were counted manually for the % of microglia exhibiting MitoEGFP expression. For 3D reconstruction of microglia and mitochondria, confocal z stacks were acquired with a 63x objective and z interval of 0.3 μm and imported into Imaris (Bit plane) software for analysis. The surface reconstruction module was used for quantification of mitochondrial and microglial volumes. For all image analyses, two or three images from separate brain sections were analyzed per mouse to obtain an average value for that mouse. Three to 7 mice were analyzed per brain region, per age and per condition. Sample sizes were selected to be in the upper range of published immunohistochemistry experiments. The filament tracer module was used

for in depth analysis of microglial morphology, with 3 to 4 microglia from separate mice reconstructed per brain region. Surfaces were also created for mitochondria from filament-traced microglia to enable linear regression analyses.

Acute brain slice preparation.

Acute slices were prepared for ex-vivo two-photon microscopy. *CX3CR1* $^{CreER/+}$*; mitoEGFP* or *CX3CR1* $^{CreER/+}$*; mitoEGFP ; Ai14* mice at 1.5 to 2.5 months were anesthetized with isoflurane and perfused transcardially with 10 ml of oxygenated, ice-cold N-methyl-D-glucamine (NMDG)-based solution containing the following (in mM): 92 NMDG, 20 HEPES, 30 NaHCO3, 1.2 NaH2PO4, 2.5 KCl, 5 sodium ascorbate, 3 sodium pyruvate, 2 thiourea, 10 MgSO4, and 0.5 CaCl2, 10 glucose, pH 7.4 (310 mOsm). Brains were then rapidly dissected free and horizontal midbrain sections (230 mm thick) and coronal forebrain sections (300 mm thick) were prepared using a vibratome in ice cold NMDG-based cutting solution bubbled continuously with 95% O2/5% CO2. Following sectioning, sections were transferred to a holding chamber containing NMDG solution at 34 ^{o}C for 5 min and then transferred to artificial cerebrospinal fluid aCSF solution at room temperature for 30 min recovery containing the following (in mM): 125 NaCl, 2.5 KCl, 1.25 NaH2PO4 2H2O, 1 MgCl2 6H2O, 26 NaHCO3, 11 Glucose and 2.4 CaCl2 2H2O and bubbled continuously with 95% 02/5% CO2.

Acute brain slice multiphoton imaging.

Acute brain slices from NAc and VTA were imaged using a Leica Stellaris 8 Dive, multiphoton microscope equipped with a Coherent Chameleon Ultra II laser and a Leica 25x/1.00 NA W motCORR objective. During video acquisition, acute brain slices were continuously perfused with aCSF bubbled with 95% 02/5% CO2. Videos were acquired at least 60 µm below the surface of the slice and video acquisition was carried out 1-3 hours after sectioning. For analysis of microglial mitochondria only (*CX3CR1* $^{CreER/+}$*; mitoEGFP* mice) an excitation wavelength of 930 nm was used and EGFP was detected via a non-descanned detector (464 - 542nm). For analysis of microglial mitochondria and microglial cell process motility (*CX3CR1* $^{CreER/+}$*; mitoEGFP ; Ai14* mice) excitation wavelength of 930 nm was again employed, to maximize MitoEGFP signal and minimize TdTom signal bleaching. MitoEGFP and TdTom signals were detected via two non descanned detectors (detector 1: 463 – 537nm, detector 2: 558 - 668nm). Stacks of images encompassing entire microglial cells (z-step interval 1 µm) were acquired at 0.02Hz (for mitochondrial motility only) and .008Hz (mitochondrial motility + microglial cell process motility). To induce a focal laser lesion, exposure to high power illumination of 750nm for 10 seconds was applied 60 µm below the surface in space surrounded by 4-5 cells. To achieve focal lesion, the zoom setting was set to max zoom available on the Leica Stellaris. Sections were imaged, zooming out of ROI to encompass 4-5 cells in the stack. Timepoints imaged post lesion included 10, 20, 50, 70 minutes. The excitation wavelength of 930 nm was again employed, to maximize MitoEGFP signal and minimize TdTom signal bleaching. MitoEGFP and TdTom signals were detected via two non descanned detectors (detector 1: 464 – 538nm, detector 2: 558 - 668nm).

Analysis of microglial and mitochondrial motility.

To analyze microglial motility, 3Dmorph, a previously published automated analysis pipeline by York et al., was adapted to analyze microglial motility[76]. For microglial motility the Td Tomato channel was used. Movies corresponding to each cell underwent preprocessing through ImageJ using previously published methodology. The video underwent background subtraction, rolling ball radius 50, and applied a median filter per 2 pixels. Then we performed z-stack projections of all movies and performed drift correction using the MultiStackReg ImageJ plugin and bleach correction using Histogram matching ImageJ plugin. An ROI around the cell of interest was created based off a max projection of time for each cell and the signal outside of ROI was removed. The Td Tomato sparse labeling made it a clear method to isolate cells. The adapted 3D morph script was applied to the final 2D movie and collected pixels added/subtracted, total pixels changed, and microglial area change. To calculate microglial motility, the total number of pixels changed after a 10 minute interval were collected and normalized to the total number of pixels making up the cell (cell area), giving a quantification of motility normalized to cell size. All analysis looked at change after a 10-minute period where microglial percent pixel change was evaluated from first time point to the nth time point (n is the frame equivalent to 10 minutes). To gain an understanding of the cell complexity, we used the Simple Neurite Tracer plugin in image j by Arshadi et al [77]. Typically used for neuronal morphology but the sholl analysis plugin was used for microglial morphology. The same preprocessing as described previously was used, additionally for the sholl analysis the first and last frame encompassing 10-minute period were used and then the output values were averaged to obtain information of cell complexity. To analyze mitochondrial motility, the isolated MitoEGFP channel movie was used. The GFP channel underwent preprocessing previously described. The 3D movie was motion corrected and the ROI created based on the Td tomato signal was applied to the EGFP channel to isolate mitochondria for corresponding cell. The video was analyzed using Imaris (Bit plane) Software. The surface reconstruction module was used to create surfaces for mitochondria in the processes which is where individual mitochondria can be easily tracked (cell bodies contain large mitochondrial networks making difficult to isolate individual mitochondria). Editing of each surface track was performed to ensure the surface was accurately visualized across time. The measurements extracted were position and volume of individual mitochondria. The position was used to calculate displacement of individual mitochondria after a 10 minute interval (like the microglial motility) and individual mitochondrial displacements were average per cell to get average mitochondrial displacement. The volume for individual mitochondria was averaged across initial frame and nth frame. The mitochondrial volume was calculated for each cell.

Tissue dissociation and flow cytometry.

2-4mo, 12-13mo, and 16-18mo WT, *CX3CR1* $^{CreER/+}$*;mitoEGFP* and *CX3CR1*$^{CreER/+}$*;TFAM*$^{Fl/Fl}$ mice were deeply anesthetized with isoflurane and

transcardially perfused with 10 ml of chilled 1M PBS. The brain was rapidly removed, cut coronally with a razor blade using anatomical landmarks and midbrain and striatum were dissected free. Samples were thoroughly minced with razor blade on a chilled glass surface and transferred to 1.7mL tubes containing 1 mL Hibernate A Low-Fluorescence (Transnetyx Tissue, Half100). Samples were then mechanically dissociated using gentle sequential trituration with fire-polished glass pipettes of decreasing diameter. Cell suspensions were pelleted via centrifugation and resuspended in 1M PBS + Debris Removal Solution (Miltenyi, 130-109-398). Debris removal was carried out according to manufacturer's instructions. Following debris removal, samples were resuspended in small volumes of 1M PBS and incubated with primary antibodies on ice for 20min. Tetramethylrhodamine (TMRM) (Biotium, 70017) was used in some experiments to assess mitochondrial membrane potential. For these experiments, samples incubated with TMRM 50nM for 20 min at room temperature, prior to the antibodies step. Following incubation, samples were washed with 1xPBS and filtered through a 35mm filter (Falcon, 352235) prior to sorting. Throughout the experiment, samples were kept at 4°C on ice. Samples were sorted using a FACS Aria I cell sorter (BD Biosciences). The population of cells containing microglia could be readily identified based on forward scattering (FSC) and side scattering (SSC) properties. A gating strategy based on FSC and SSC width and height was used to select single cells and reduce dead cells and doublets. Microglial cells within this population were then identified and sorted based on combinations of microglial antibodies. Antibody combinations used included anti-CD45 (1:400; Biolegend, 147703), anti-P2RY12 (1:500; Biolegend, 848005), and anti-CX3CR1 (1:800; Biolegend, 149023). Gated Microglia were FACS sorted into 1.7mL tubes containing 50µl Pico Pure RNA extraction buffer and, following the sort, samples were incubated at 42°C for 30 min, and stored in RNase-free tubes at -80°C until further processing.

RNA Extraction and qPCR.

Total RNA was extracted from sorted cells using Pico Pure RNA isolation kit (Arcturus Bioscience) according to the manufacturer's instructions. Single strand cDNAs were synthesized using Superscript III first-strand cDNA synthesis kit (Invitrogen, 18080051), according to the manufacturer's protocol. Samples were subjected to PreAmplification-RT-PCR method based on previously published approaches. TaqMan PreAmp Master Mix Kit was used for cDNA preamplification (Cat# 4391128; Applied Biosystems, Life Technologies), using pooled primer mixes of 20x dilution of TaqMan Gene Expression Assay and 80 nM of custom-designed primer sets. cDNAs were pre-amplified in an Veriti 96-Well Fast Thermal Cycler (ThermoFisher Scientific, 4375305) using the program: 95°C hold for 10 min, 14 cycles of 90°C denaturation for 15 s, and 60°C annealing and extension for 4 min. Pre-amplification PCR products were immediately diluted five times with molecular biology grade water and stored at -20°C, or immediately processed for RT-PCR. For qPCR analysis of gene expression, single plex qPCR assays were performed on technical duplicates using TaqMan probes for each gene target or for endogenous control gene (*Gapdh*). TaqMan Advanced Fast PCR

Master Mix was used (catalog #4444963; Invitrogen). To avoid amplification of any genomic DNA contamination, primers and probes that amplify across target gene exon–exon junctions were selected when possible. qPCRs reactions were run in a QuantStudio5 using the program: 95°C hold for 20 s, followed by 40 cycles of 95°C denaturation for 3 s, and 60°C annealing and extension for 30 s. Calculations of relative expression from Ct data were conducted according to User Bulletin #23898 for ABI Prism 7900 Sequence Detection System. For each target gene, the average Ct value for the endogenous control (*Gapdh*) was subtracted from the average Ct value for the TaqMan Probe per target gene, to obtain DCt. The relative expression was then plotted as 2^{-DCt}. All TaqMan Assays and custom primers/probes that were used are detailed in Table S5.

Statistical analyses.

Data analysis was performed in OriginPro and R. Heatmaps were generated in R using the ComplexHeatmap package by Gu Z et al [78]. PCAs were generated in R using the ggplot2 package by Wickham H, 2016 [79]. Linear regression analysis for LPS experiments were performed in R, all other linear regression analysis was performed in OriginPro. Cumulative distributions were generated using OriginPro or Matlab and analyzed using Kolmogorov-Smirnov tests. All graphed values are shown as mean ±SEM. Statistical details of experiments (statistical tests used, exact value of n, what n represents) can be found in Results and the figure legends. In general, statistical significance was assessed using one- or two-way ANOVA. Post hoc comparisons were conducted using Student's t test with Bonferroni correction for multiple comparisons. Data are sufficiently normal and variance within groups is sufficiently similar for use of parametric tests. 2 tailed paired t tests were used to compare trends across two different regions within individual mice.

References

1. Li, Q. & Barres, B. A. Microglia and macrophages in brain homeostasis and disease. *Nat. Rev. Immunol.* **18**, 225–242 (2018).
2. Sierra, A., Paolicelli, R. C. & Kettenmann, H. Cien Años de Microglía: Milestones in a Century of Microglial Research. *Trends Neurosci.* **42**, 778–792 (2019).
3. Matsudaira, T. & Prinz, M. Life and death of microglia: Mechanisms governing microglial states and fates. *Immunol. Lett.* **245**, 51–60 (2022).
4. Grabert, K. *et al.* Microglial brain region−dependent diversity and selective regional sensitivities to aging. *Nat. Neurosci.* **19**, 504–516 (2016).

5. Stowell, R. D. *et al.* Cerebellar microglia are dynamically unique and survey Purkinje neurons in vivo. *Dev. Neurobiol.* **78**, 627–644 (2018).
6. Paolicelli, R. C. *et al.* Microglia states and nomenclature: A field at its crossroads. *Neuron* **110**, 3458–3483 (2022).
7. Böttcher, C. *et al.* Human microglia regional heterogeneity and phenotypes determined by multiplexed single-cell mass cytometry. *Nat. Neurosci.* **22**, 78–90 (2019).
8. De Biase, L. M. & Bonci, A. Region-Specific Phenotypes of Microglia: The Role of Local Regulatory Cues. *The Neuroscientist* **25**, 314–333 (2019).
9. Ayata, P. *et al.* Epigenetic regulation of brain region-specific microglia clearance activity. *Nat. Neurosci.* **21**, 1049–1060 (2018).
10. Hanamsagar, R. & Bilbo, S. D. Environment matters: microglia function and dysfunction in a changing world. *Curr. Opin. Neurobiol.* **47**, 146–155 (2017).
11. Salter, M. W. & Stevens, B. Microglia emerge as central players in brain disease. *Nat. Med.* **23**, 1018–1027 (2017).
12. Wolf, S. A., Boddeke, H. W. G. M. & Kettenmann, H. Microglia in Physiology and Disease. *Annu. Rev. Physiol.* **79**, 619–643 (2017).
13. Gleichman, A. J. & Carmichael, S. T. Glia in neurodegeneration: Drivers of disease or along for the ride? *Neurobiol. Dis.* **142**, 104957 (2020).
14. Ceasrine, A. M. & Bilbo, S. D. Dietary fat: a potent microglial influencer. *Trends Endocrinol. Metab. TEM* **33**, 196–205 (2022).
15. Sequeira, M. K. & Bolton, J. L. Stressed Microglia: Neuroendocrine-Neuroimmune Interactions in the Stress Response. *Endocrinology* **164**, bqad088 (2023).

16. Wangler, L. M. & Godbout, J. P. Microglia moonlighting after traumatic brain injury: aging and interferons influence chronic microglia reactivity. *Trends Neurosci.* **46**, 926–940 (2023).
17. Hickman, S. E. *et al.* The microglial sensome revealed by direct RNA sequencing. *Nat. Neurosci.* **16**, 1896–1905 (2013).
18. Madry, C. & Attwell, D. Receptors, ion channels, and signaling mechanisms underlying microglial dynamics. *J. Biol. Chem.* **290**, 12443–12450 (2015).
19. Zengeler, K. E. & Lukens, J. R. Microglia pack a toolbox for life. *Trends Immunol.* **45**, 338–345 (2024).
20. Davalos, D. *et al.* ATP mediates rapid microglial response to local brain injury in vivo. *Nat. Neurosci.* **8**, 752–758 (2005).
21. Nimmerjahn, A., Kirchhoff, F. & Helmchen, F. Resting Microglial Cells Are Highly Dynamic Surveillants of Brain Parenchyma in Vivo. *Science* **308**, 1314–1318 (2005).
22. Eyo, U. B. & Wu, L.-J. Microglia: Lifelong patrolling immune cells of the brain. *Prog. Neurobiol.* **179**, 101614 (2019).
23. Shen, K. *et al.* Mitochondria as Cellular and Organismal Signaling Hubs. *Annu. Rev. Cell Dev. Biol.* **38**, 179–218 (2022).
24. Collier, J. J., Oláhová, M., McWilliams, T. G. & Taylor, R. W. Mitochondrial signalling and homeostasis: from cell biology to neurological disease. *Trends Neurosci.* **46**, 137–152 (2023).
25. Picard, M. & Shirihai, O. S. Mitochondrial signal transduction. *Cell Metab.* **34**, 1620–1653 (2022).

26. Tan, J. X. & Finkel, T. Mitochondria as intracellular signaling platforms in health and disease. *J. Cell Biol.* **219**, e202002179 (2020).
27. Kolliniati, O., Ieronymaki, E., Vergadi, E. & Tsatsanis, C. Metabolic Regulation of Macrophage Activation. *J. Innate Immun.* **14**, 51–68 (2021).
28. Mills, E. L. & O'Neill, L. A. Reprogramming mitochondrial metabolism in macrophages as an anti-inflammatory signal. *Eur. J. Immunol.* **46**, 13–21 (2016).
29. Mills, E. L. *et al.* Succinate Dehydrogenase Supports Metabolic Repurposing of Mitochondria to Drive Inflammatory Macrophages. *Cell* **167**, 457-470.e13 (2016).
30. Diskin, C. & Pålsson-McDermott, E. M. Metabolic Modulation in Macrophage Effector Function. *Front. Immunol.* **9**, 270 (2018).
31. Ramond, E., Jamet, A., Coureuil, M. & Charbit, A. Pivotal Role of Mitochondria in Macrophage Response to Bacterial Pathogens. *Front. Immunol.* **10**, 2461 (2019).
32. Wang, Y., Li, N., Zhang, X. & Horng, T. Mitochondrial metabolism regulates macrophage biology. *J. Biol. Chem.* **297**, 100904 (2021).
33. Afroz, S. F. *et al.* Mitochondrial dynamics in macrophages: divide to conquer or unite to survive? *Biochem. Soc. Trans.* **51**, 41–56 (2023).
34. De Biase, L. M. *et al.* Local Cues Establish and Maintain Region-Specific Phenotypes of Basal Ganglia Microglia. *Neuron* **95**, 341-356.e6 (2017).
35. Maes, M. E. *et al.* Mitochondrial network adaptations of microglia reveal sex-specific stress response after injury and UCP2 knockout. *iScience* **26**, 107780 (2023).
36. Bordt, E. A. *et al.* Gonadal hormones impart male-biased behavioral vulnerabilities to immune activation via microglial mitochondrial function. *Brain. Behav. Immun.* **115**, 680–695 (2024).

37. Baik, S. H. *et al.* A Breakdown in Metabolic Reprogramming Causes Microglia Dysfunction in Alzheimer's Disease. *Cell Metab.* **30**, 493-507.e6 (2019).
38. March-Diaz, R. *et al.* Hypoxia compromises the mitochondrial metabolism of Alzheimer's disease microglia via HIF1. *Nat. Aging* **1**, 385–399 (2021).
39. Fecher, C. *et al.* Cell-type-specific profiling of brain mitochondria reveals functional and molecular diversity. *Nat. Neurosci.* **22**, 1731–1742 (2019).
40. Agarwal, A. *et al.* Transient Opening of the Mitochondrial Permeability Transition Pore Induces Microdomain Calcium Transients in Astrocyte Processes. *Neuron* **93**, 587-605.e7 (2017).
41. Yona, S. *et al.* Fate Mapping Reveals Origins and Dynamics of Monocytes and Tissue Macrophages under Homeostasis. *Immunity* **38**, 79–91 (2013).
42. Faust, T. E. *et al.* A comparative analysis of microglial inducible Cre lines. *Cell Rep.* **42**, 113031 (2023).
43. Bedolla, A. M. *et al.* A comparative evaluation of the strengths and potential caveats of the microglial inducible CreER mouse models. *Cell Rep.* **43**, 113660 (2024).
44. Madisen, L. *et al.* A robust and high-throughput Cre reporting and characterization system for the whole mouse brain. *Nat. Neurosci.* **13**, 133–140 (2010).
45. Lou, N. *et al.* Purinergic receptor P2RY12-dependent microglial closure of the injured blood-brain barrier. *Proc. Natl. Acad. Sci. U. S. A.* **113**, 1074–1079 (2016).
46. Etienne, F. *et al.* Two-photon Imaging of Microglial Processes' Attraction Toward ATP or Serotonin in Acute Brain Slices. *J. Vis. Exp. JoVE* (2019) doi:10.3791/58788.
47. Bernier, L.-P. *et al.* Microglial metabolic flexibility supports immune surveillance of the brain parenchyma. *Nat. Commun.* **11**, 1559 (2020).

48. Norden, D. M., Trojanowski, P. J., Villanueva, E., Navarro, E. & Godbout, J. P. Sequential activation of microglia and astrocyte cytokine expression precedes increased Iba-1 or GFAP immunoreactivity following systemic immune challenge. *Glia* **64**, 300–316 (2016).
49. Nair, S. *et al.* Lipopolysaccharide-induced alteration of mitochondrial morphology induces a metabolic shift in microglia modulating the inflammatory response in vitro and in vivo. *Glia* **67**, 1047–1061 (2019).
50. Park, J. *et al.* Mitochondrial dynamics modulate the expression of pro-inflammatory mediators in microglial cells. *J. Neurochem.* **127**, 221–232 (2013).
51. Orihuela, R., McPherson, C. A. & Harry, G. J. Microglial M1/M2 polarization and metabolic states. *Br. J. Pharmacol.* **173**, 649–665 (2016).
52. Hu, Y. *et al.* mTOR-mediated metabolic reprogramming shapes distinct microglia functions in response to lipopolysaccharide and ATP. *Glia* **68**, 1031–1045 (2020).
53. O'Neill, L. A. J., Kishton, R. J. & Rathmell, J. A guide to immunometabolism for immunologists. *Nat. Rev. Immunol.* **16**, 553–565 (2016).
54. Van den Bossche, J. *et al.* Mitochondrial Dysfunction Prevents Repolarization of Inflammatory Macrophages. *Cell Rep.* **17**, 684–696 (2016).
55. Hoogland, I. C. M., Houbolt, C., van Westerloo, D. J., van Gool, W. A. & van de Beek, D. Systemic inflammation and microglial activation: systematic review of animal experiments. *J. Neuroinflammation* **12**, 114 (2015).
56. Su, É., Villard, C. & Manneville, J.-B. Mitochondria: At the crossroads between mechanobiology and cell metabolism. *Biol. Cell* **115**, e2300010 (2023).

57. Picard, M., Shirihai, O. S., Gentil, B. J. & Burelle, Y. Mitochondrial morphology transitions and functions: implications for retrograde signaling? *Am. J. Physiol.-Regul. Integr. Comp. Physiol.* **304**, R393–R406 (2013).
58. Candlish, M. & Hefendehl, J. K. Microglia Phenotypes Converge in Aging and Neurodegenerative Disease. *Front. Neurol.* **12**, 660720 (2021).
59. Brawek, B., Skok, M. & Garaschuk, O. Changing Functional Signatures of Microglia along the Axis of Brain Aging. *Int. J. Mol. Sci.* **22**, 1091 (2021).
60. Niraula, A., Sheridan, J. F. & Godbout, J. P. Microglia Priming with Aging and Stress. *Neuropsychopharmacol. Off. Publ. Am. Coll. Neuropsychopharmacol.* **42**, 318–333 (2017).
61. Moca, E. N. *et al.* Microglia Drive Pockets of Neuroinflammation in Middle Age. *J. Neurosci.* **42**, 3896–3918 (2022).
62. Liu, H. *et al.* TFAM is an autophagy receptor that limits inflammation by binding to cytoplasmic mitochondrial DNA. *Nat. Cell Biol.* **26**, 878–891 (2024).
63. Larsson, N. G. *et al.* Mitochondrial transcription factor A is necessary for mtDNA maintenance and embryogenesis in mice. *Nat. Genet.* **18**, 231–236 (1998).
64. Fornasiero, E. F. *et al.* Precisely measured protein lifetimes in the mouse brain reveal differences across tissues and subcellular fractions. *Nat. Commun.* **9**, 4230 (2018).
65. Alshial, E. E. *et al.* Mitochondrial dysfunction and neurological disorders: A narrative review and treatment overview. *Life Sci.* **334**, 122257 (2023).
66. Norat, P. *et al.* Mitochondrial dysfunction in neurological disorders: Exploring mitochondrial transplantation. *NPJ Regen. Med.* **5**, 22 (2020).

67. Bame, X. & Hill, R. A. Mitochondrial network reorganization and transient expansion during oligodendrocyte generation. *Nat. Commun.* **15**, 6979 (2024).

68. Zehnder, T. *et al.* Mitochondrial biogenesis in developing astrocytes regulates astrocyte maturation and synapse formation. *Cell Rep.* **35**, 108952 (2021).

69. Fairley, L. H. *et al.* Mitochondrial control of microglial phagocytosis by the translocator protein and hexokinase 2 in Alzheimer's disease. *Proc. Natl. Acad. Sci. U. S. A.* **120**, e2209177120 (2023).

70. Hope, K. T., Hawes, I. A., Moca, E. N., Bonci, A. & De Biase, L. M. Maturation of the microglial population varies across mesolimbic nuclei. *Eur. J. Neurosci.* **52**, 3689–3709 (2020).

71. Harrington, J. S., Ryter, S. W., Plataki, M., Price, D. R. & Choi, A. M. K. Mitochondria in health, disease, and aging. *Physiol. Rev.* **103**, 2349–2422 (2023).

72. König, T. & McBride, H. M. Mitochondrial-derived vesicles in metabolism, disease, and aging. *Cell Metab.* **36**, 21–35 (2024).

73. Yona, S. *et al.* Fate Mapping Reveals Origins and Dynamics of Monocytes and Tissue Macrophages under Homeostasis. *Immunity* **38**, 79–91 (2013).

74. Agarwal, A. *et al.* Transient Opening of the Mitochondrial Permeability Transition Pore Induces Microdomain Calcium Transients in Astrocyte Processes. *Neuron* **93**, 587-605.e7 (2017).

75. Madisen, L. *et al.* A robust and high-throughput Cre reporting and characterization system for the whole mouse brain. *Nat. Neurosci.* **13**, 133–140 (2010).

76. York, E. M., LeDue, J. M., Bernier, L.-P. & MacVicar, B. A. 3DMorph Automatic Analysis of Microglial Morphology in Three Dimensions from Ex Vivo and In Vivo Imaging. *eNeuro* **5**, ENEURO.0266-18.2018 (2018).

77. Arshadi, C., Günther, U., Eddison, M., Harrington, K. I. S. & Ferreira, T. A. SNT: a unifying toolbox for quantification of neuronal anatomy. *Nat. Methods* **18**, 374–377 (2021).

78. Gu, Z., Eils, R. & Schlesner, M. Complex heatmaps reveal patterns and correlations in multidimensional genomic data. *Bioinforma. Oxf. Engl.* **32**, 2847–2849 (2016).

79. Wickham, H. *Ggplot2*. (Springer International Publishing, Cham, 2016). doi:10.1007/978-3-319-24277-4.

Author Contributions

K.E., A.W.S., and L.M.D. designed research; K.E., A.W.S., A.S., K.M., M.Y., and C.C. performed research; K.E., A.W.S., D.T.G., A.S., K.M., M.Y., and C.C. analyzed data; K.E., A.W.S., and L.M.D edited the paper, K.E. and A.W.S wrote the first draft of the paper, K.E. and A.W.S. wrote the paper; L.M.D supervised research

Acknowledgements

This work was supported by the Diana Jacobs Kalman Scholarship (American Federation on Aging Research scholarship to A.W.S), the Jennifer S. Buchwald Graduate Fellowship (UCLA Department of Physiology fellowship to K.E.), a University of California Office of the President Pre-Professoriate Fellowship (to K.E.), UCLA CARE Summer Undergraduate Fellowship (to C.C.), UCLA CARE Summer Undergraduate Fellowship (to K.M.), David Geffen School of Medicine at UCLA start-up funds (to L.M.D.) and a Stanley Fahn Junior Faculty Award (PF-SF-JFA-836586; Parkinson's Foundation Grant to L.M.D.). We thank the UCLA Eli and Edythe Broad Center of Regenerative Medicine and Stem Cell Research Flow Cytometry Core and the UCLA Jonsson Comprehensive Cancer Center and Center for AIDS Research Flow Cytometry Core for assistance with FACS-based experiments. We thank the UCLA Eli and Edythe Broad Center of Regenerative Medicine and Stem Cell Research Microscopy Core for access to and use of confocal microscopes and Imaris workstations. We thank Dr. Elaine Hsiao for use of the Hsiao lab QuantStudio5 for qPCR experiments. We thank Dr. Fanny Etienne for assistance with training for multiphoton imaging experiments.

FIGURES AND FIGURE LEGENDS

Figure 1

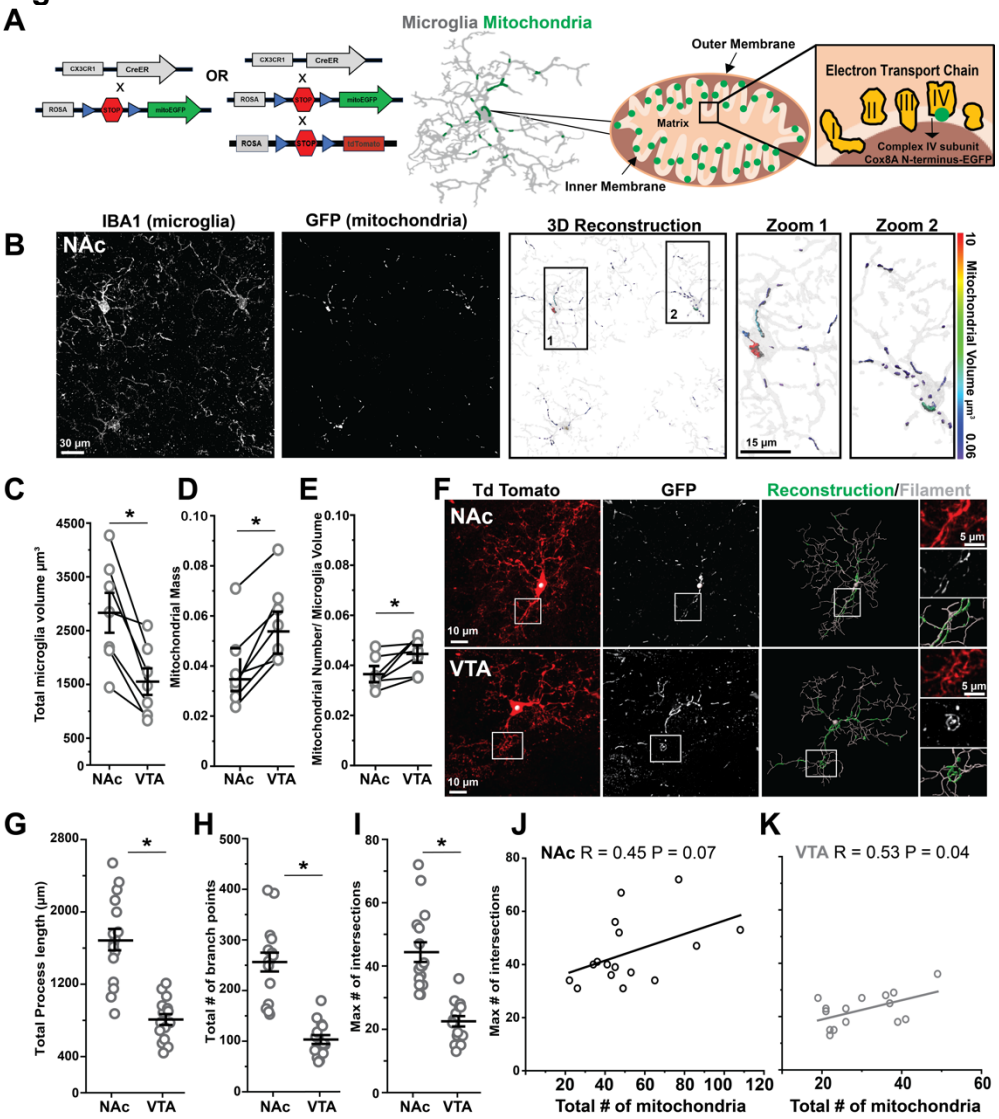

L

Morphological Parameters	Region	Total # of Mito	Total Vol. of Mito (µm³)
Total Process Length (µm)	NAc	R=0.14 P=0.59	*R=0.49 P=0.05*
	VTA	**R=0.48 P=0.06**	**R=0.44 P=0.09**
# of microglial branch pts.	NAc	R=0.13 P=0.61	**R=0.45 P=0.07**
	VTA	*R=0.56 P=0.02*	**R=0.49 P=0.06**
Max # of intersections	NAc	**R=0.45 P=0.07**	R=0.34 P=0.19
	VTA	*R=0.53 P=0.04*	R=0.43 P=0.10

FIGURE 1: Regional specialization of microglia is accompanied by regional differences in mitochondrial mass and number. (A) Schematic of transgenic crosses used to achieve GFP labeling of microglial mitochondria. **(B)** Representative high-magnification images at P60 of NAc microglia (Iba1) and mitochondria (GFP); panels *at right* show 3D reconstructions of microglia (*transparent gray*) and mitochondria (colored according to volume). **(C-E)** Quantification of microglia volume (tissue coverage), mitochondrial mass (mitochondrial volume / microglial volume), and mitochondrial

number (relative to cell volume) in NAc and VTA. Data points from the same mouse are identified by the connecting line (P60 N = 7 mice NAc and VTA). *C.* paired t-test p = 0.003 *D.* paired t-test p = 0.001 *E.* paired t-test p = 0.026. **(F)** Representative confocal images of microglial cells in NAc and VTA expressing cytosolic TdTom and mitochondrial targeted GFP (*MG-mitoGFP;Ai14* mice). Reconstruction of cell branching via filament-tracing in Imaris along with 3D reconstruction of mitochondria is shown *at right*. **(G-I)** Morphological parameters individual microglia derived from filament tracing and Sholl analysis (P60 NAc N = 16 cells and VTA N = 15 cells). *G.* Two-sample t-test p<0.0001 *H.* Two-sample t-test p<0.0001 *I.* Two-sample t-test p<0.0001. **(J-K)** Linear regression plots showing relationships between mitochondrial number and microglial morphological complexity as measured by max # of Sholl intersections. **(L)** Table containing statistics for all linear regression analyses performed.

FIGURE 2

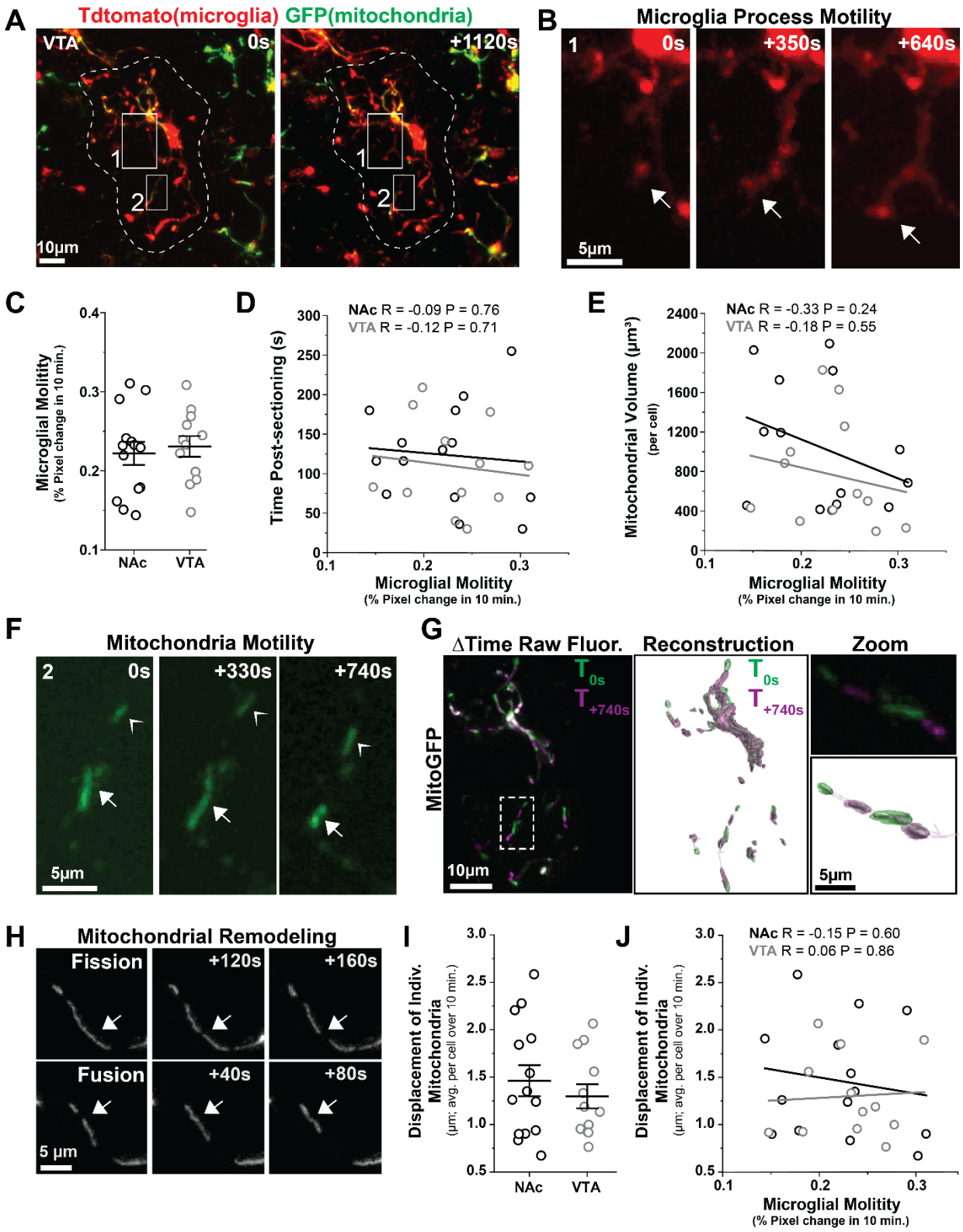

FIGURE 2: Mitochondrial abundance and mitochondrial motility are not strongly correlated with microglial tissue surveillance. (A) Representative images of

multiphoton live imaging of VTA microglia (Td Tomato) in acute brain sections from 1.5 - 2mo old mice. **(B)** Example of microglial cell process extension indicated by *white arrow*. **(C)** Quantification of microglial motility over a 10- minute period in two regions NAc and VTA. Two sample t-test p=0.659, n.s. **(D)** Linear regression analysis of microglial motility (% pixel change over time), and time elapsed since preparation of acute brain sections. **(E)** Linear regression analysis of relationships between mitochondrial volume (total volume in cell averaged across time points to account for dynamic changes in mitochondrial volume) and microglial motility over a 10-minute period. **(F)** Representative images of multiphoton live imaging of VTA mitochondria (EGFP) in acute brain sections from 1.5-2mo old mice. **(G)** Raw fluorescence from multiphoton imaging (*left*) and 3D reconstruction of microglial mitochondria (*right*) colored by time. **(H)** Representative examples of mitochondrial fission and fusion observed in microglia from young adult mice. **(I)** Quantification of displacement of individual mitochondria averaged within a cell over a 10-minute period in NAc and VTA. Two-sample t-test p=0.447, n.s. **(J)** Linear regression analysis of relationships between displacement of individual mitochondria per cell versus microglial motility for NAc and VTA microglia (N=14 NAc microglia and N=12 VTA microglia).

FIGURE 3

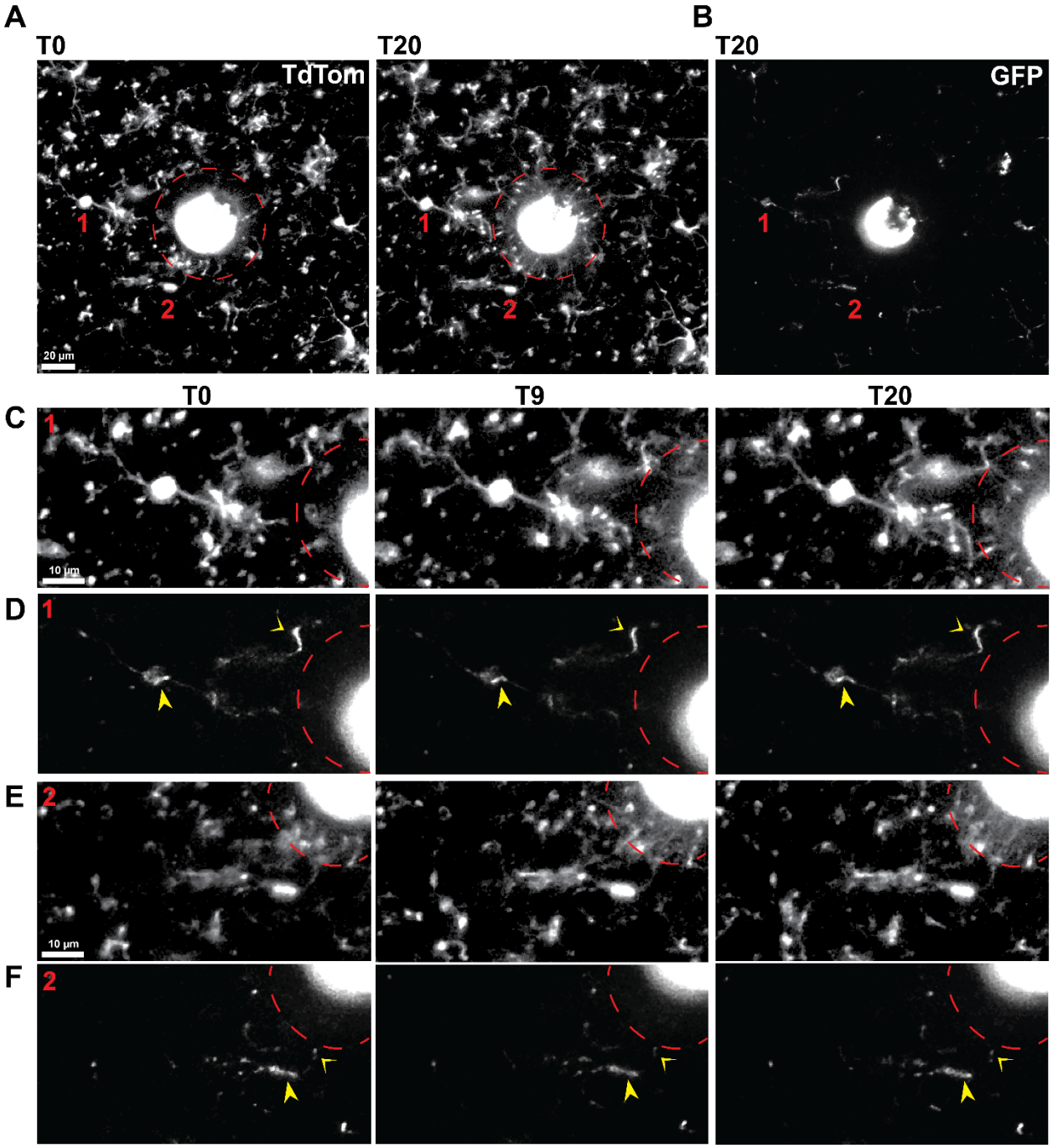

FIGURE 3: Mitochondrial distribution is stable during early phases of microglial response to focal injury. **(A)** Representative video of microglia in an acute brain slice from young adult *MG-mitoGFP;Ai14* mouse responding to focal laser lesion. **(B)** Representative image of mitochondria in an acute brain slice from young adult *MG-mitoGFP;Ai14* mouse responding to focal laser lesion. **(C,E)** Higher magnification images of two microglia that extend cell processes toward the lesion while their

mitochondrial networks (GFP) remain stable. Red enclosed circle defining territory near lesion. **(D,F)** Two higher magnification images of two cells with mitochondria (GFP). Red enclosed circle defining territory near lesion and arrows (closed – soma mitochondria, open – process mitochondria) pointing to mitochondria. Number of FOVs imaged = 7 NAc slices (3 animals).

FIGURE 4

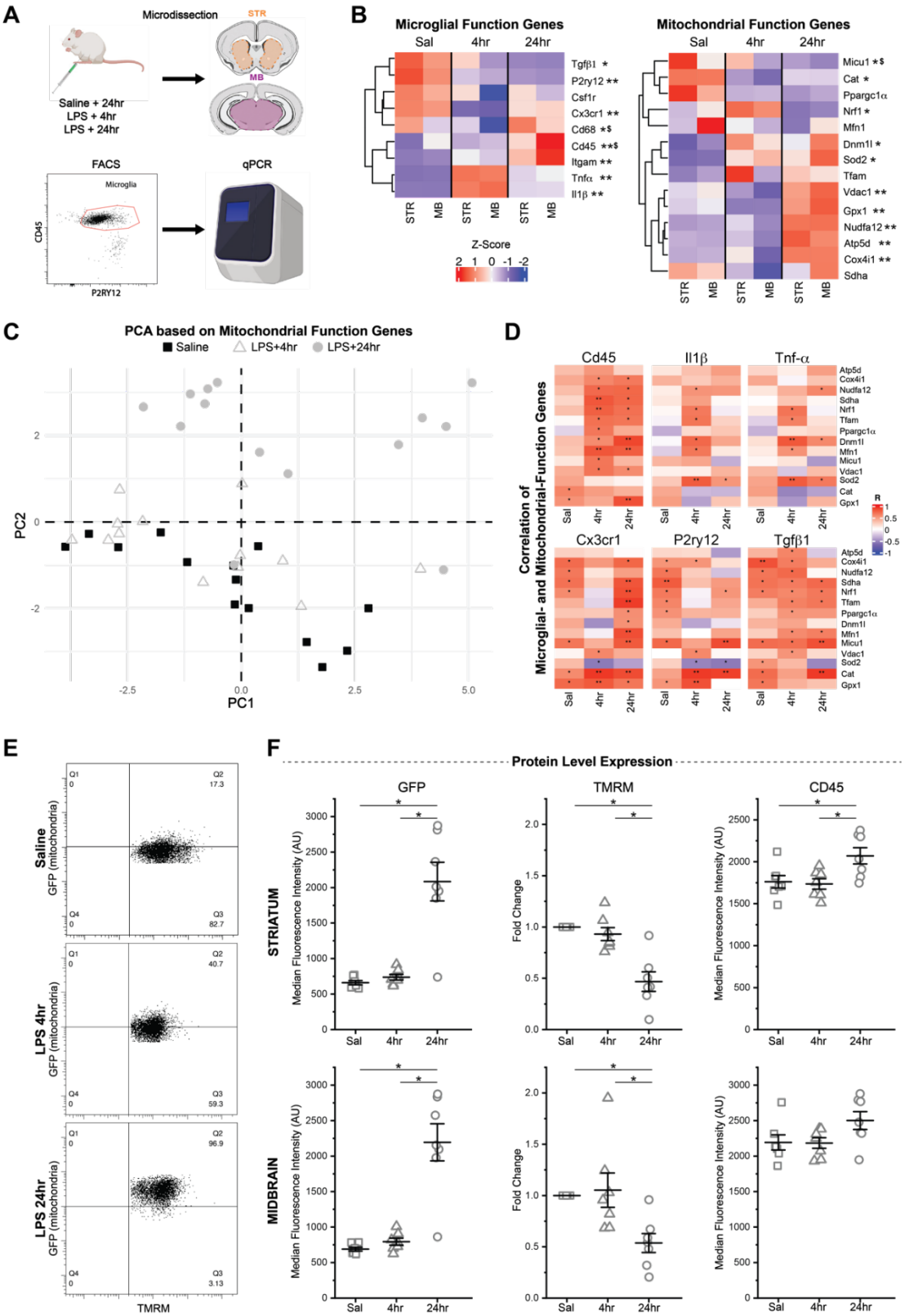
A
Microdissection
STR
MB
Saline + 24hr
LPS + 4hr
LPS + 24hr
FACS
Microglia
CD45
P2RY12
qPCR
B
Microglial Function Genes
Sal
4hr
24hr
Tgfβ1 *
P2ry12 **
Csf1r
Cx3cr1 **
Cd68 *$
Cd45 **$
Itgam **
Tnfα **
Il1β **
STR
MB
Z-Score
2 1 0 -1 -2
Mitochondrial Function Genes
Micu1 *$
Cat *
Ppargc1α
Nrf1 *
Mfn1
Dnm1l *
Sod2 *
Tfam
Vdac1 **
Gpx1 **
Nudfa12 **
Atp5d **
Cox4i1 **
Sdha
C
PCA based on Mitochondrial Function Genes
Saline
LPS+4hr
LPS+24hr
PC2
PC1
-2.5
0.0
2.5
5.0
D
Cd45
Il1β
Tnf-α
Cx3cr1
P2ry12
Tgfβ1
Correlation of
Microglial- and Mitochondrial-Function Genes
Atp5d
Cox4i1
Nudfa12
Sdha
Nrf1
Tfam
Ppargc1α
Dnm1l
Mfn1
Micu1
Vdac1
Sod2
Cat
Gpx1
Sal
4hr
24hr
R
1
0.5
0
-0.5
-1
E
Saline
LPS 4hr
LPS 24hr
GFP (mitochondria)
TMRM
Q1
Q2
Q3
Q4
17.3
82.7
40.7
59.3
96.9
3.13
F
Protein Level Expression
GFP
TMRM
CD45
STRIATUM
MIDBRAIN
Median Fluorescence Intensity (AU)
Fold Change
Sal
4hr
24hr

Figure 4: Response to inflammatory challenge (LPS) elicits rapid mitochondrial changes in microglia. (A) Schematic of experiment design. 3-4mo *MG-MitoEGFP* mice were injected with saline 24hr prior to or LPS 4hr or 24hr prior FACS isolation of STR/MB microglia for downstream qPCR analysis. **(B)** Heatmaps showing expression levels of key microglial function and mitochondrial function genes in each group. Z-scores represent average gene expression across treatment groups and brain regions. See *Tables S1* and *S2* for F- and P-values. (N = 7 Saline STR, N = 7 Saline MB, N = 7 LPS 4hr STR, N = 6 LPS 4hr MB, N = 7 LPS 24hr STR, N = 7 LPS MB). **(C)** PC1 and PC2 of Principal Component Analysis of samples using only mitochondrial function genes. **(D)** Heatmaps depicting the correlation of pro-inflammatory (*Cd45*, *Il1b*, *Tnf-a*) and homeostatic (*Cx3cr1*, *P2ry12*, *Tgfb1*) microglial function genes with mitochondrial function genes as determined by linear regression analysis. See *Table S3* for R- and P-values. **(E)** Representative dot plots of FACS analyzed Saline, LPS 4hr, and LPS 24hr microglia comparing TMRM fluorescence intensity to GFP fluorescence intensity. **(F)** Quantification of Median Fluorescence Intensity of GFP, TMRM (individual cell TMRM signal was normalized to the same cell's GFP signal to account for mitochondrial mass), and CD45 signal in STR and MB microglia from Saline (N =7), LPS 4hr (N=7), and LPS 24hr (N = 7) mice. One-way ANOVA: GFP STR, $F_{(2,18)} = 25.06735$, $p < 0.0001$; GFP MB, $F_{(2,18)} = 29,85264$, $p < 0.0001$; TMRM STR, $F_{(2,18)} = 19.2316$, $p < 0.0001$; TMRM MB, $F_{(2,18)} = 6.61021$, $p = 0.00704$; CD45 STR, $F_{(2,18)} = 5.52274$, $p = 0.01348$; CD45 MB, $F_{(2,18)} = 2.99003$, $p = 0.07565$. * $P < 0.05$, t-test with Bonferroni correction.

FIGURE 5

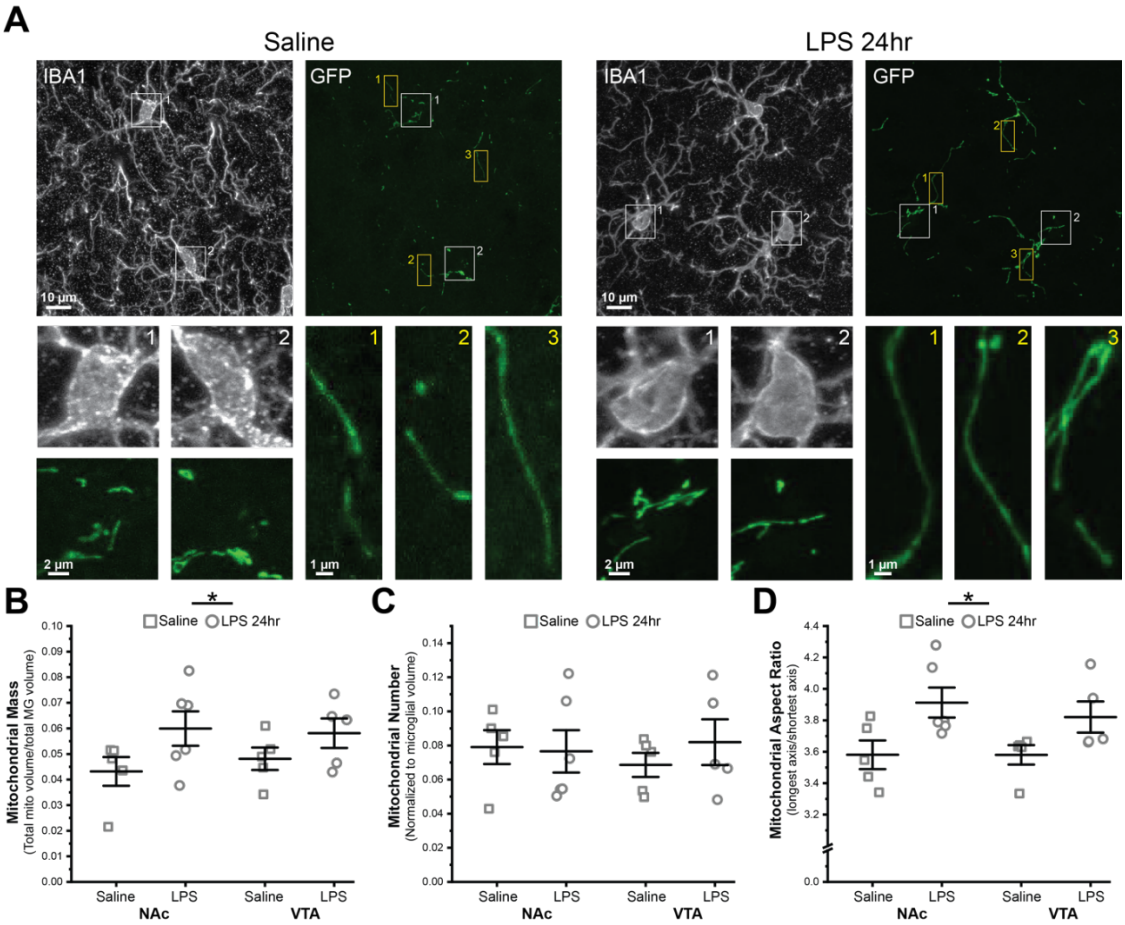

Figure 5: Microglial responses to inflammatory challenge (LPS) are accompanied by microglial elongation and increases mitochondrial mass. (A) Representative images of NAc microglia (IBA1) and their mitochondria (GFP) from 3-4mo *MG-MitoEGFP* mice injected with saline (*left*) or LPS 24hr (*right*). *White* and *yellow boxes* highlight microglial somas and cell processes where higher magnification zooms are shown *below*. **(B)** Quantification of microglial mitochondrial mass (mitochondrial volume / cell volume; Two-way ANOVA: main effect of treatment, $F_{(1,17)} = 5.19787$, p-value = 0.03579; main effect of region, $F_{(1,17)} = 0.0713$, p-value = 0.079266). **(C)** Quantification of mitochondrial number (relative to cell volume; Two-way ANOVA: main effect of treatment, $F_{(1,17)} = .23167$, p-value = 0.63642; main effect of region, $F_{(1,17)} = 0.05079$, p-value = 0.82438). **(D)** Quantification of mitochondrial aspect ratio (longest axis / shortest axis; Two-way ANOVA: main effect of treatment, $F_{(1,17)} = 10.19319$, p-value = 0.00533; main effect of region, $F_{(1,17)} = 0.26571$, p-value = 0.61286). N = 5-6 mice per group.

FIGURE 6

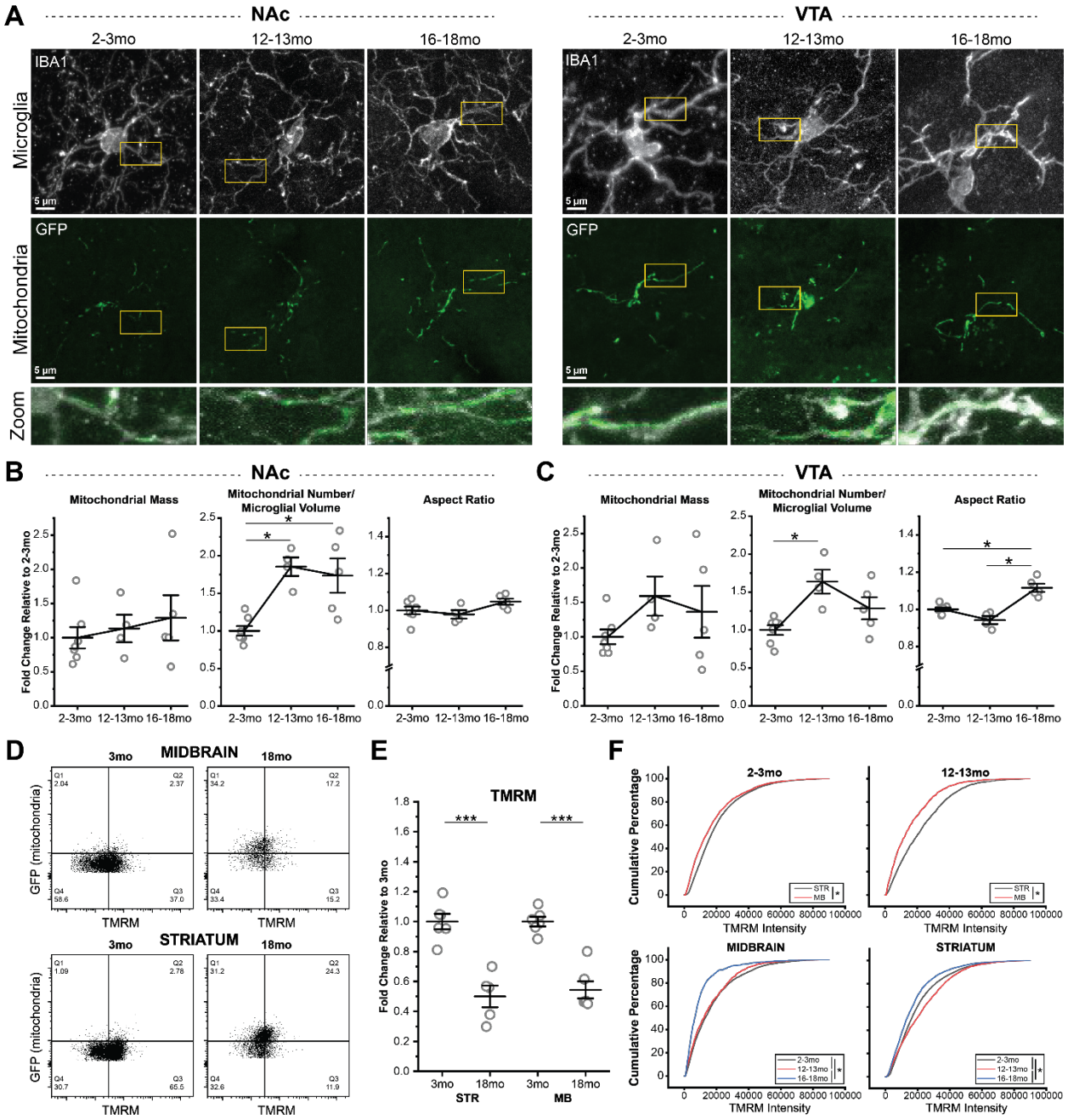

Figure 6: Microglial mitochondria undergo remodeling in middle- and late middle age. (A) Representative images of NAc (*left*) and VTA (*right*) microglia (IBA1) and microglial mitochondria (GFP) from 2-3mo, 12-13mo, and 16-18mo *MG-MitoEGFP* mice. (B-C) Mitochondrial mass, number, and aspect ratio of NAc (B) and VTA (C) microglia during aging, normalized to mean values from 2-3mo animals. Statistical comparisons were made using one-way ANOVAs and two sample t-test with Bonferonni correction. * P < 0.05. (D) Representative dot plots from FACS analysis of 2-3mo and 16-18mo MG-MitoEGFP microglia showing TMRM fluorescence intensity (measure of

mitochondrial membrane potential) and GFP fluorescence intensity. (E) Median fluorescence intensity of TMRM (individual cell TMRM signal was normalized to the same cell's GFP signal to account for mitochondrial mass) from the STR and MB of 3mo (N = 6 STR, 6 MB) and 18mo (N = 5 STR, 6 MB) animals. Statistical comparisons were made using two-way ANOVAs and two sample t-test with Bonferonni correction. *** $P < 0.001$. (F) Cumulative probability distribution of TMRM fluorescence intensity of 2-3mo microglia (*top left*) and 12-13mo microglia (*top right*) and midbrain microglia (*bottom left*) and striatum microglia (*bottom right*) from 2-3mo, 12-13mo, and 16-18mo mice. Kolmogorov-Smirnov tests comparing ages within each region show that distributions at each age are significantly different from one another. * $P < 0.05$.

FIGURE 7

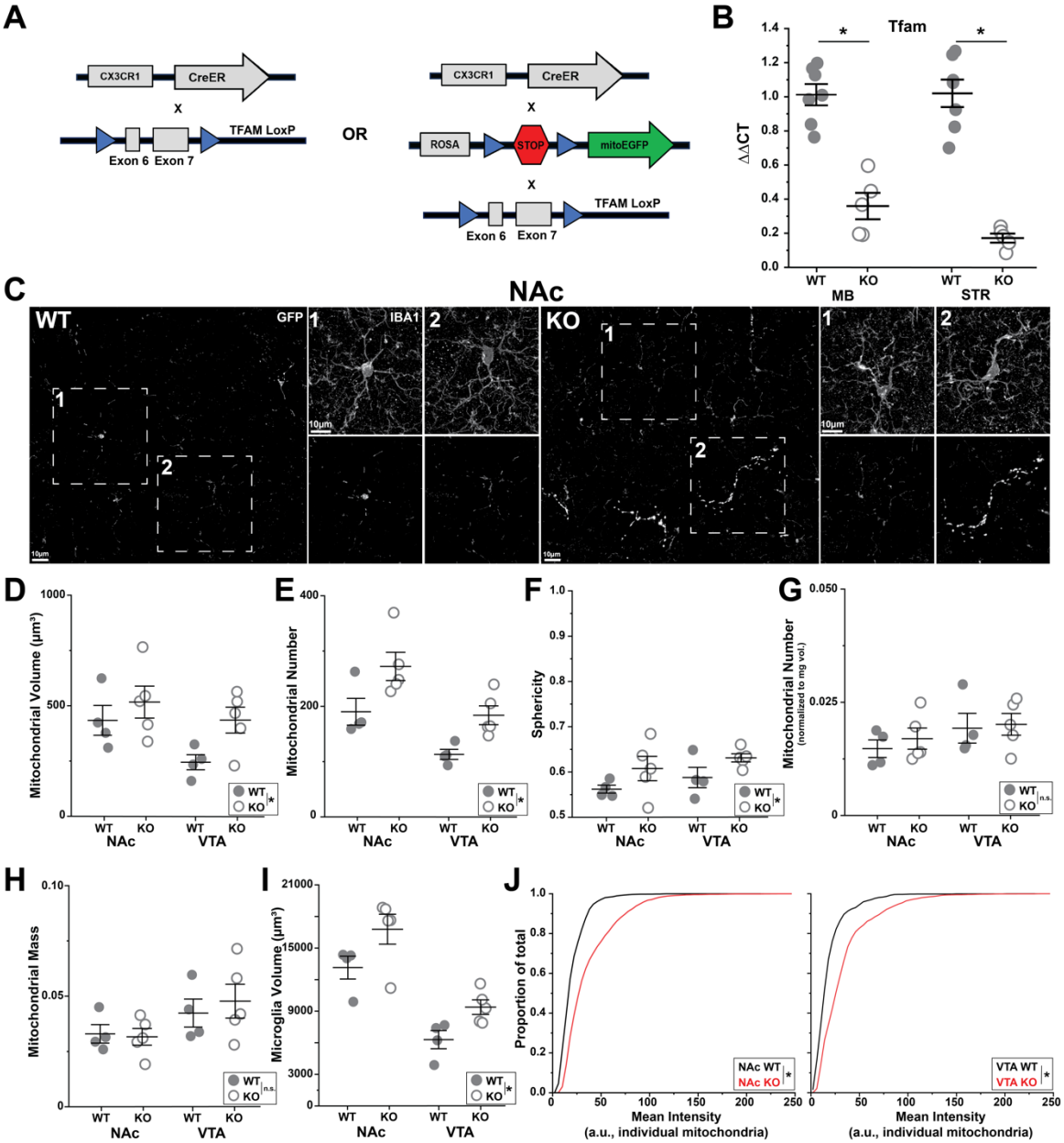

Figure 7: Mitochondria display altered morphology after TFAM downregulation

(A) Schematic of transgenic crosses used to achieve disruption of mitochondria in microglia and labeling of mitochondria. **(B)** Quantification of relative expression of transcription factor A (TFAM) in FACs isolated microglia in both MB and STR (fold change ΔΔCT), two-way Anova Genotype F = 115.410 p <0.0001, Region F = 1.654 p = 0.213. **(C)** Representative high-magnification images at 5 mos. of NAc microglia (Iba1) and mitochondria (GFP) in both WT control and TFAM KO mice. **(D)** Quantification of mitochondrial volume, two-way Anova Genotype F = 4.808 p = 0.046, Region F = 4.716 p = 0.046. **(E)** Quantification of mitochondrial number, two-way Anova Genotype F = 13.489 p = 0.002, Region F = 15.864 p = 0.0013. **(F)** Quantification of mitochondrial

sphericity, two-way Anova Genotype $F = 5.313$ $p = 0.037$, Region $F = 1.636$ $p = 0.221$. **(G)** Quantification of mitochondrial number normalized to microglial volume, two-way Anova Genotype $F = 0.366$ $p = 0.554$, Region $F = 2.295$ $p = 0.152$, n.s. **(H)** Quantification of mitochondrial mass, two-way Anova Genotype $F= 0.119$ $p = 0.734$, Region $F = 4.728$ $p = 0.047$, n.s. **(I)** Quantification of microglial volume across NAc and VTA in WT and TFAM KO mice, two-way Anova Genotype $F = 9.665$ $p = 0.007$, Region $F = 43.274$ $p<0.0001$. WT = 4 mice and KO = 5 mice. **(J)** Cumulative distribution of mean intensity for individual mitochondria across FOV in both WT and TFAM KO mice in NAc and VTA. *J.* NAc WT = 2124 mitochondria KO = 4063 mitochondria, Kolmogorov-Smirnov test $p<0.0001$ *C.*VTA WT = 1468 mitochondria KO = 2684 mitochondria, Kolmogorov-Smirnov test $p=0.0015$.

FIGURE 8

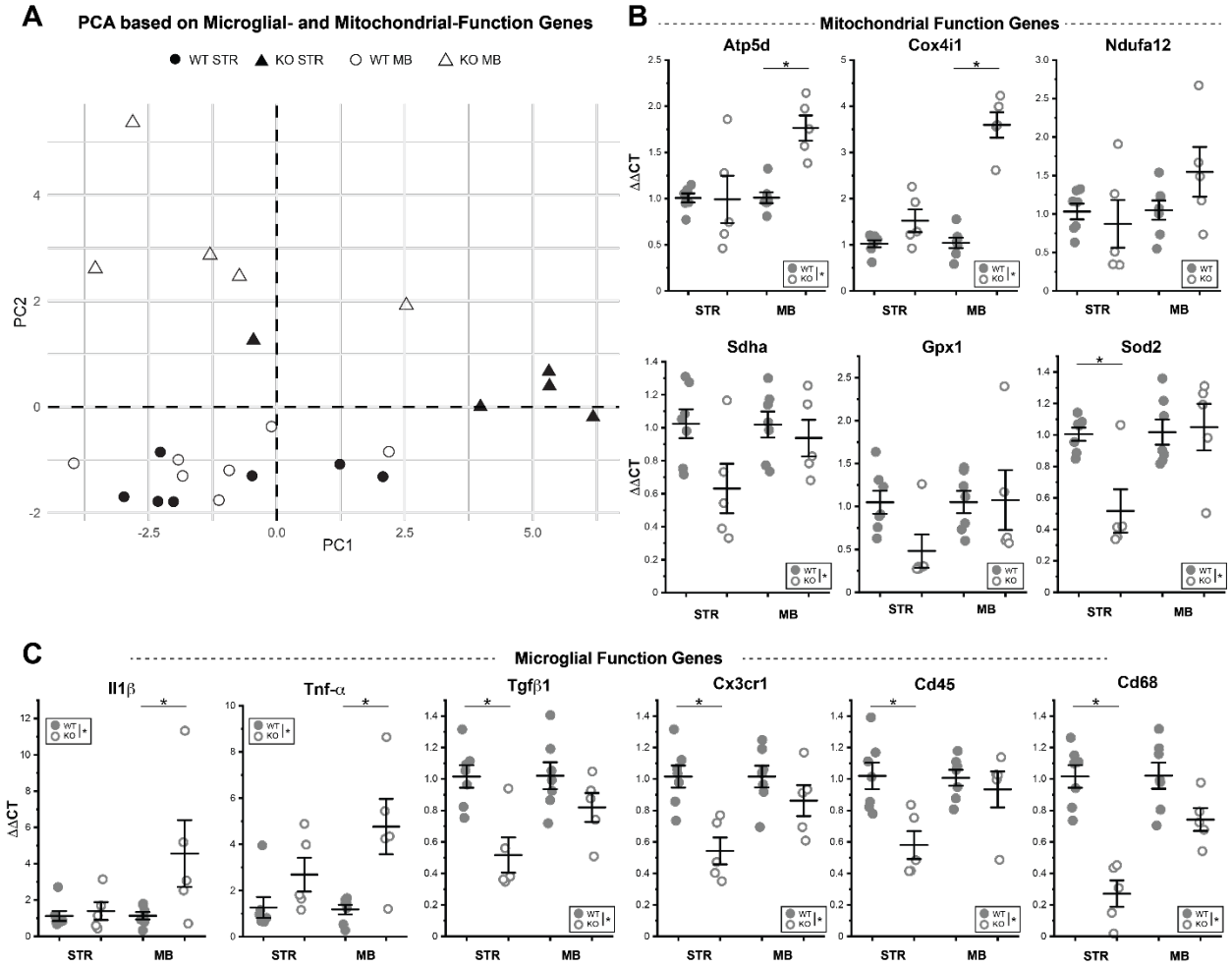

(A) Principal Component Analysis of control and MG-TFAMKO samples based on microglial- and mitochondrial- function related genes along PC1 and PC2. **(B and C)** Quantification of normalized, relative expression (fold change or ΔΔCT) of mitochondrial function genes **(B)** and microglial function genes **(C)** from FACs isolated MB and STR microglia using qPCR. See Table 5 for ANOVA and Post Hoc analysis values.

SUPPLEMENTARY FIGURE 1

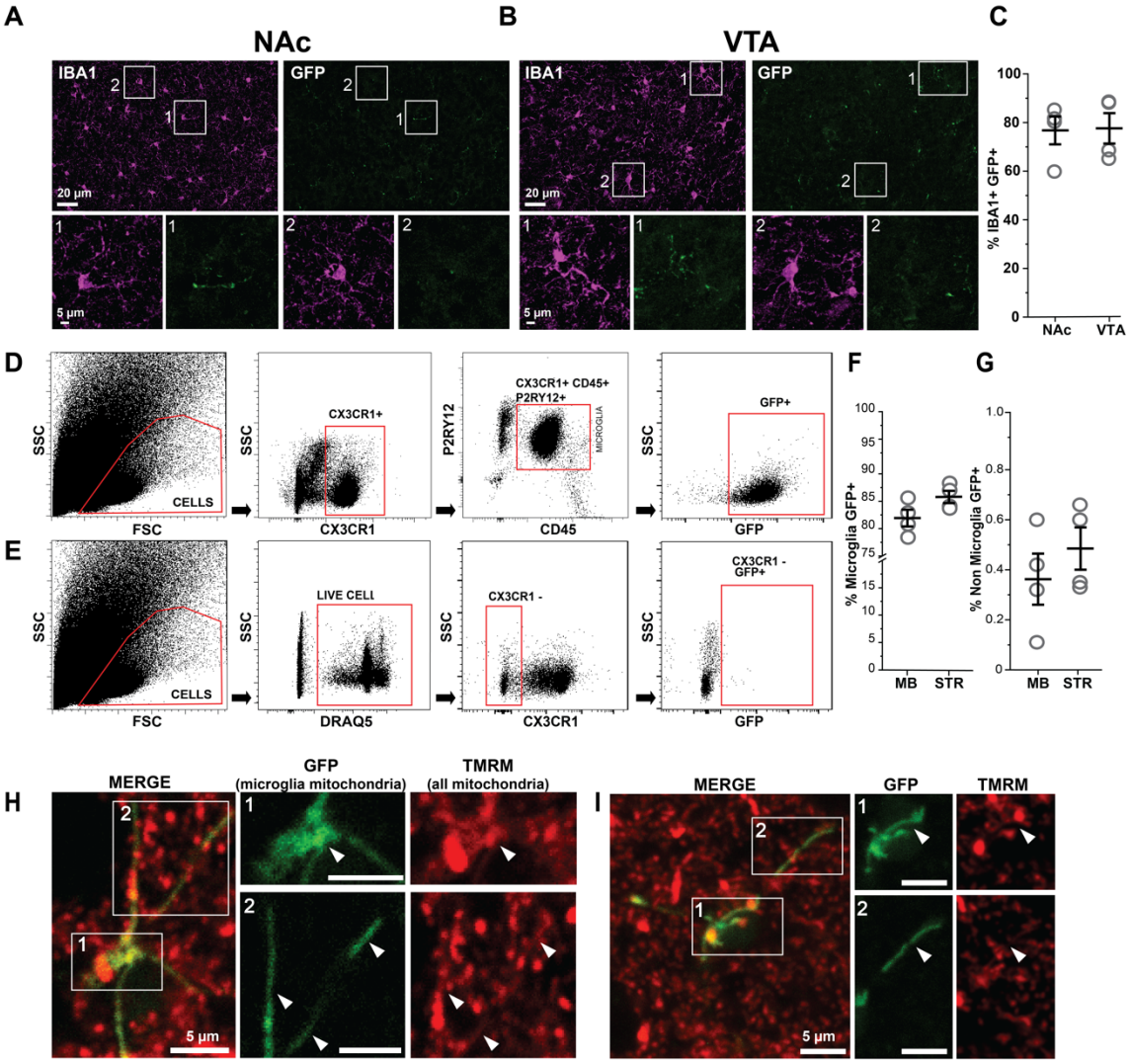

FIGURE S1: Validation of *CX3CR1-CreER; flox-stop mitoEGFP* (*MG-MitoEGFP*) mice. (A) 20x confocal images of native EGFP signal and Iba1 (magenta) staining in *CX3CR1-CreER; flox-stop mitoEGFP* (*MG-MitoEGFP*) mice showing that all EGFP labeled mitochondria are within Iba1+. Box 1 and 2 examples of IBA1+ GFP+ positive cells and IBA1+GFP- cells. **(B)** Showing native EGFP signal in VTA. **(C)** Quantification of percentage of microglia showing recombination and expression of EGFP in mitochondria in nucleus accumbens (NAc) and ventral tegmental area (VTA). N= 4 mice NAc and VTA. **(D)** FACS-based analysis in midbrain (MB) and striatum (STR) of percentage of microglia showing recombination. Sequential gating strategy shown, CX3CR1+P2RY12+CD45+ putative microglia isolated and GFP+ gate shown. **(E)** Gating strategy for live cells (DRAQ5+), non-microglia (CX3CR1-) and GFP+ shown. **(F-G)** Percentage of microglia (CX3CR1+P2RY12+CD45+) and non-microglial cells (CX3CR1- Draq5+) showing expression of GFP in MB and STR. N= 4 mice MB and

STR. **(H-I)** Live imaging of acute brain sections from *MG-MitoEGFP* mice incubated with mitochondrial membrane potential indicator dye TMRM. Examples 1 and 2 show co-labeling of GFP and TMRM. Zoom 1 shows cell body colocalization and zoom 2 shows colocalization in the processes.

SUPPLEMENTARY FIGURE 2

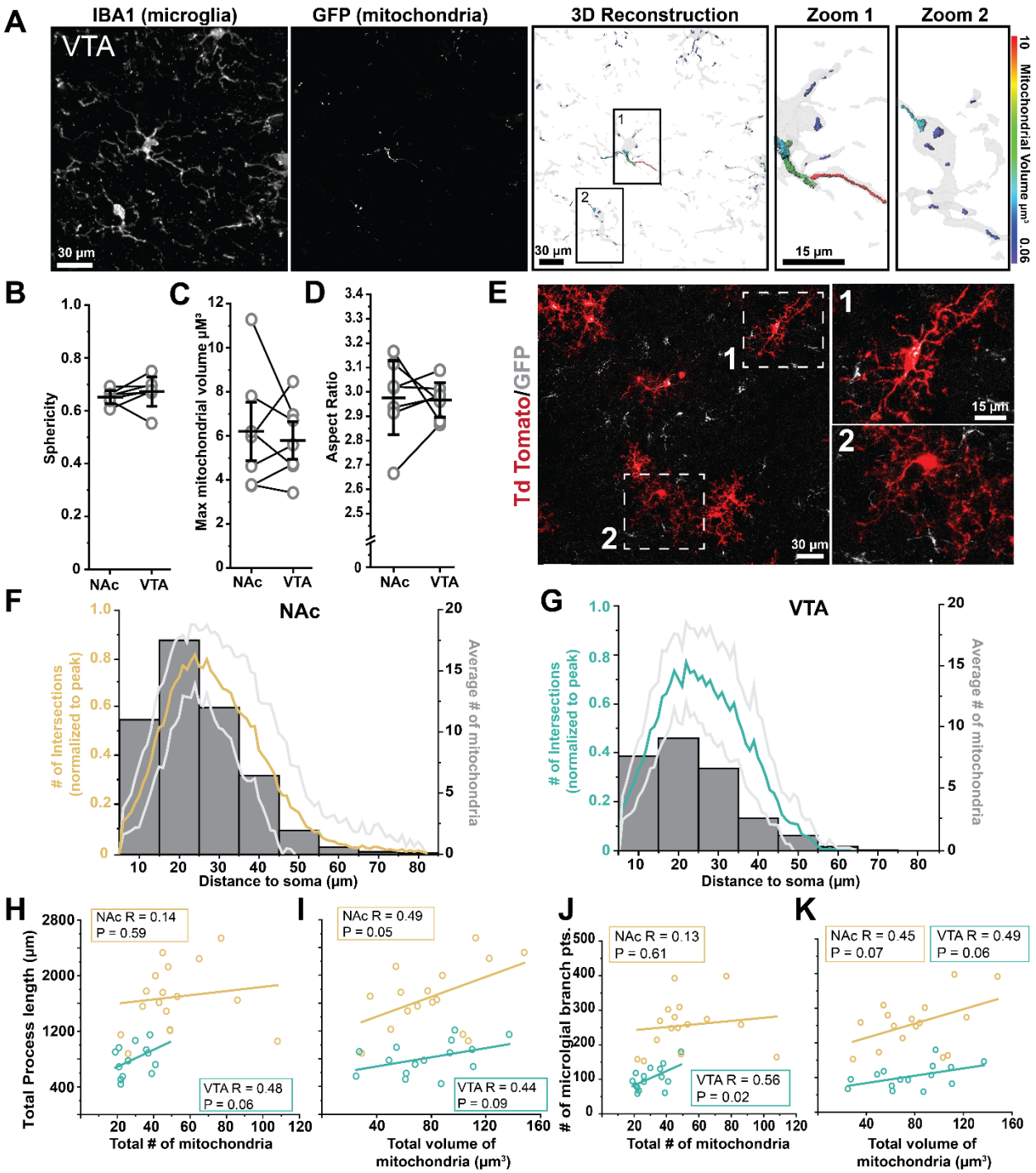

FIGURE S2: Mitochondrial morphology network changes are heterogeneous in microglia (continuation Fig.1) (A) Representative high-magnification images at P60 of NAc microglia (Iba1) and mitochondria (EGFP); 3D reconstructions of mitochondria (colored according to volume) and zoomed in panels (1 and 2) on bottom left depicting colocalized surfaces. **(B-D)** Quantification of mitochondrial parameters at P60 across regions (NAc, VTA). Within a given age, data points that come from the same mouse

are identified by the connecting line (P60 N = 7 mice NAc and VTA). *B.* paired t-test sphericity p = 0.346, n.s. *C.* paired t-test max mitochondria volume p = 0.640, n.s. *D.* paired t-test aspect ratio (long axis divided by short axis) p = 0.894, n.s. **(E)** Representative 20x image of TdTom and mitoEGFP sparse labeling. **(F-G)** Sholl analysis of individual reconstructed microglia; normalized to peak and averaged across regions (P60 NAc N = 16 cells and VTA N = 15 cells). **(H-K)** Linear regression plots for showing relationships between microglial process length and mitochondrial morphological parameters for both regions (P60 NAc N = 16 cells and VTA N = 15 cells).

SUPPLEMENTARY FIGURE 3

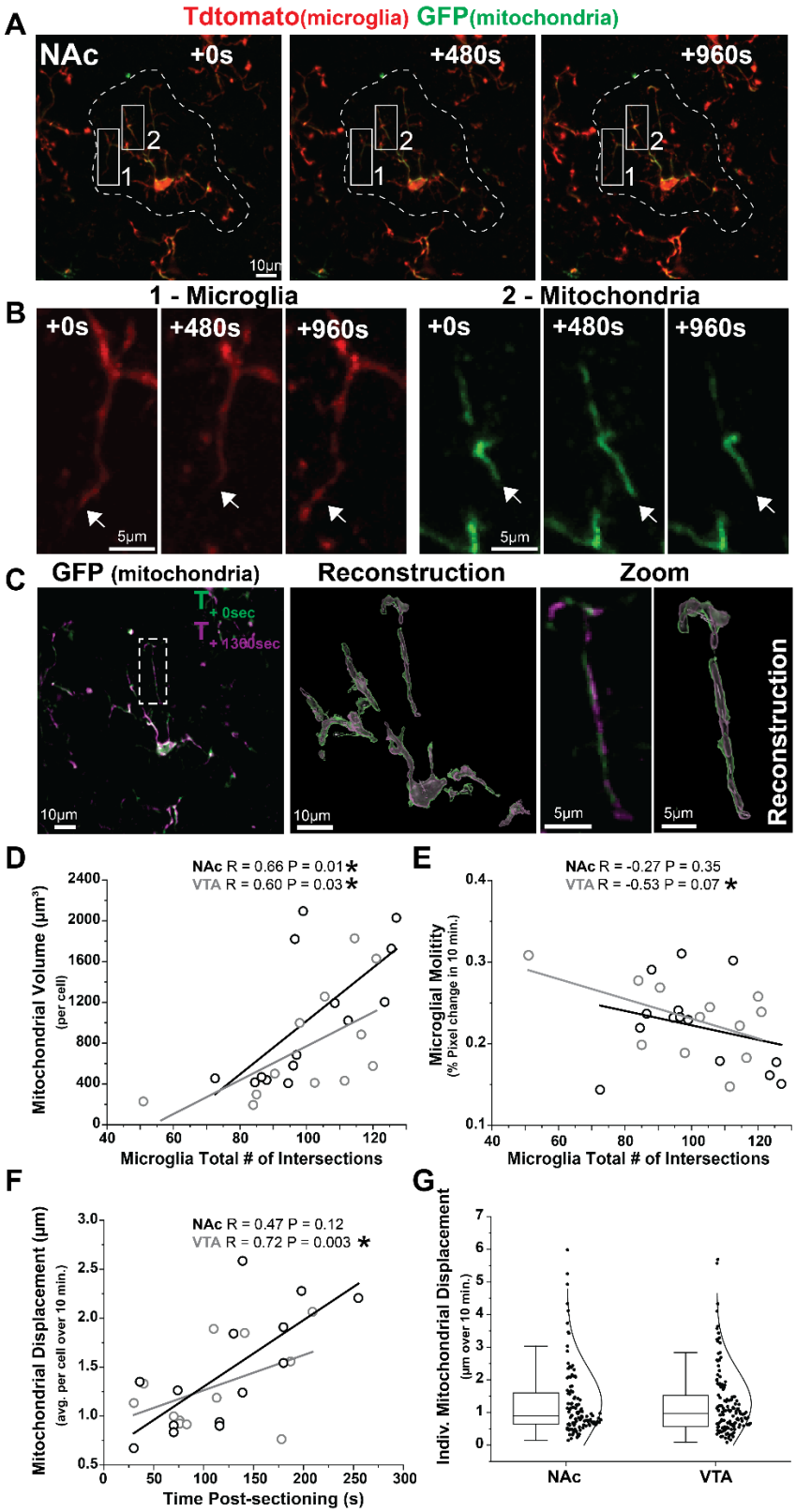

FIGURE S3: Microglial mitochondria present dynamic motility and network remodeling. (related to Fig.2). (A) Representative images of first frame and last frame of acute brain slice of NAc microglia (Td Tomato) and mitochondria (EGFP) at 1.5-2mos old mice. **(B)** Example of microglia process retraction/extension and mitochondrial displacement indicated by white arrow at different timepoints. **(C)** 3D reconstructions of mitochondria (colored by time frame) and zoomed in panels on right depicting fluorescence and respective surface reconstruction. **(D)** Linear regression plot showing relationship between mitochondrial total volume per cell and Sholl analysis based microglial number of intersections. NAc $R = 0.66$ $p = 0.01$, VTA $R = 0.60$ $p = 0.03$. **(E)** Linear regression plot showing relationship between microglial motility and Sholl analysis based microglial number of intersections. NAc $R = -0.27$ $p = 0.35$ VTA $R = -0.53$ $p = 0.07$. **(F)** Linear regression plot showing relationship between displacement of individual mitochondria per cell and time post-sectioning. NAc $R = 47$ $p = 0.12$ VTA $R = 0.72$ $p = 0.003$. **(G)** Distribution plot of individual mitochondria displacement in NAc and VTA over a 10-minute period (NAc N = 116 mitochondria VTA N = 134 mitochondria).

SUPPLEMENTARY FIGURE 4

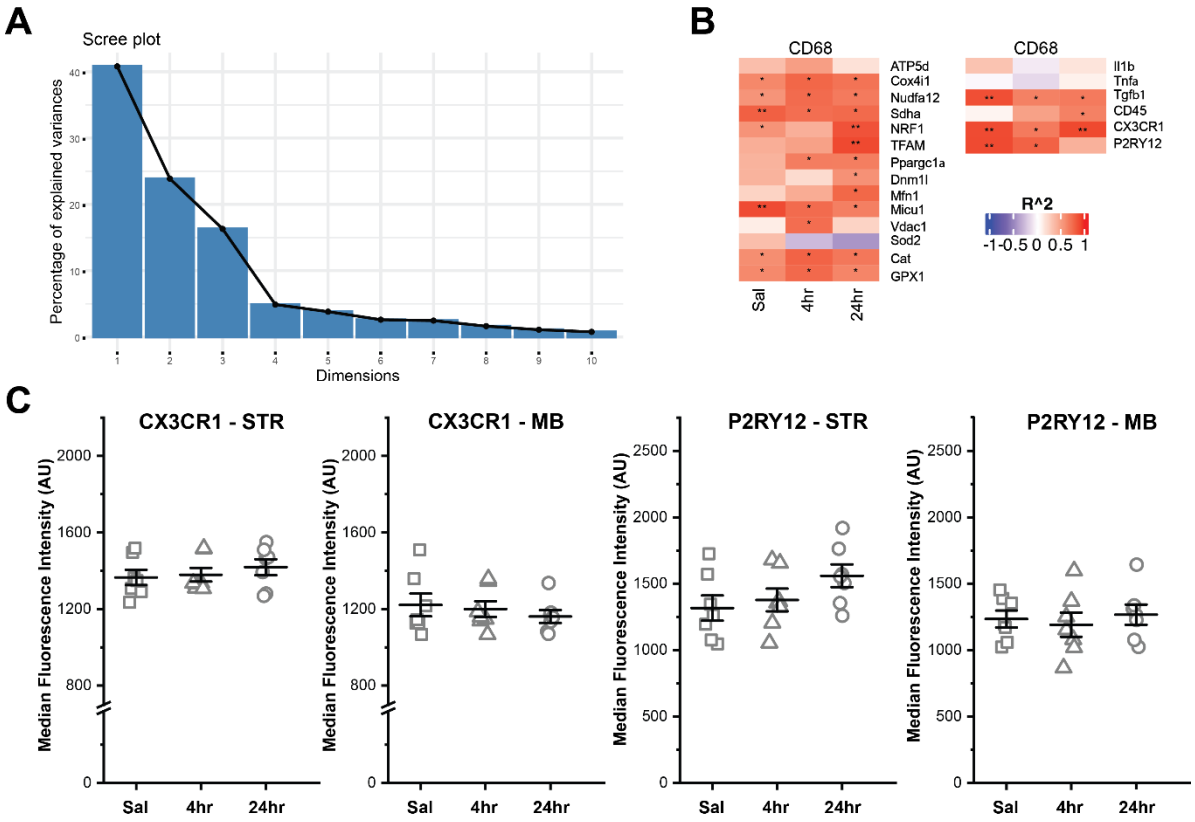

Figure S4: Microglial and mitochondrial responses to inflammatory challenge (LPS), related to Fig 4. (A) Scree plot describing the percentage of explained variance for the Principal Component Analysis of saline, LPS 4hr, and LPS 24hr samples based only on mitochondrial function genes. **(B)** Heat maps depicting the correlation of Cd68 with microglial function genes and mitochondrial function genes as analyzed by linear regression. See Supp Table 1 for R2- and P-values. **(C)** Quantification of Median Fluorescent Intensity of CX3CR1 and P2RY12 signal in the STR and MB of Saline (N =7), LPS 4hr (N=7), and LPS 24hr (N = 7) samples. Samples are not significantly different by treatment but were significantly different by region. Two-way ANOVA: CX3CR1 Treatment, $F(2,36) = 0.00442$, $p = 0.99559$, Region, $F(1,36) = 30.80804$, $p < 0.0001$; P2RY12 Treatment, $F(2,36) = 1.71502$, $p = 0.19514$, Region $F(1,36) = 7.52567$, $p = 0.00942$.

SUPPLEMENTARY FIGURE 5

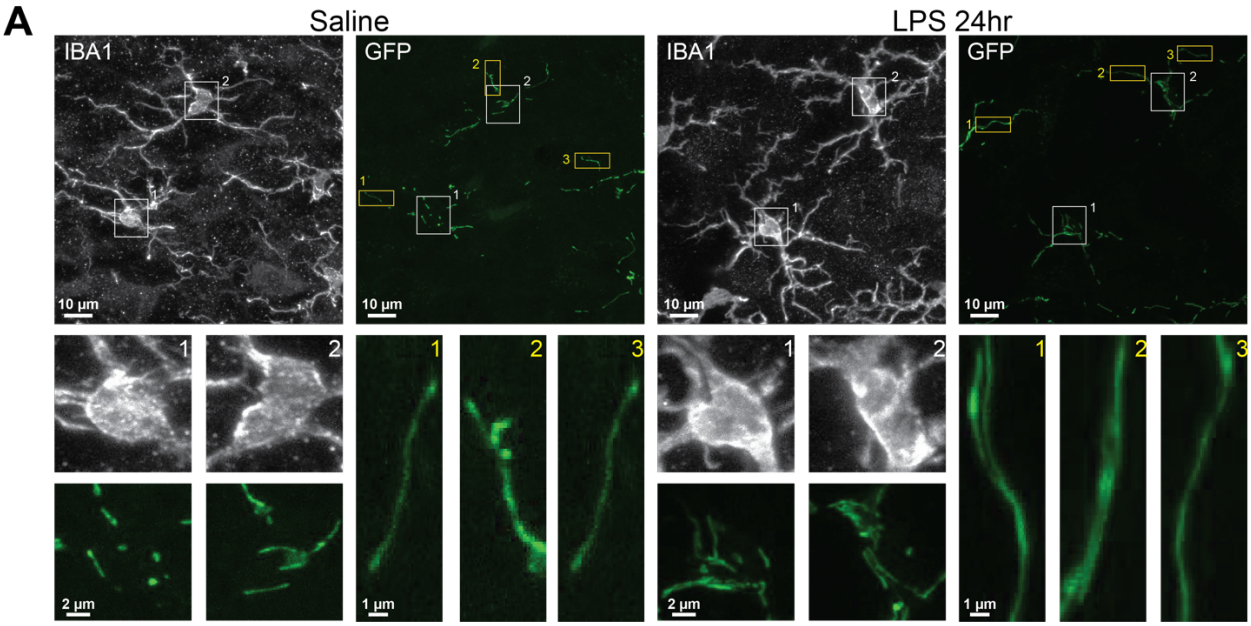

Figure S5: VTA microglial mitochondrial response to inflammatory challenge (LPS, related to Fig 5). **(A)** Representative images of VTA microglia (IBA1) and microglial mitochondria (GFP) of 3-4mo *MG-MitoEGFP* mice injected with saline (left) or LPS 24hr (right) prior to euthanasia. Zoomed panels depict example somatic mitochondria (white frame) and cell process mitochondria (yellow frame).

SUPPLEMENTARY FIGURE 6

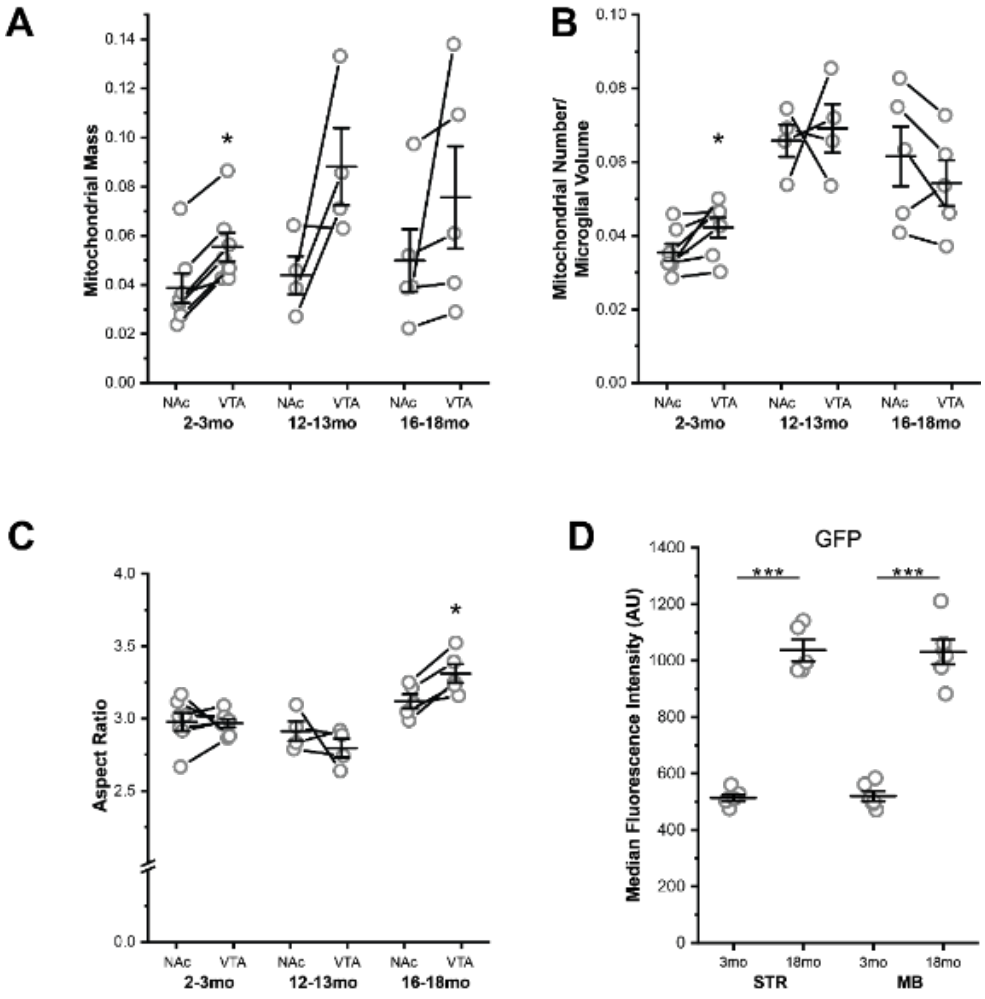

Figure S6: Microglial mitochondria undergo remodeling in middle- and late middle age (related to Fig. 6). (A-C) Comparison of NAc and VTA microglial mitochondrial mass **(A)**, mitochondrial number normalized to microglial volume **(B)**, and mitochondrial aspect ratio **(C)** from individual 2-3mo, 12-13mo, and 16-18mo mice. * $p < 0.05$, two tailed, paired t-test. **(D)** Median fluorescence intensity of GFP from the STR and MB of 3mo (N = 6 STR, 6 MB) and 18mo (N = 5 STR, 6 MB) animals. Statistical comparisons were made using two-way ANOVAs and two sample t-test with Bonferonni correction. *** $P < 0.001$.

SUPPLEMENTARY FIGURE 7

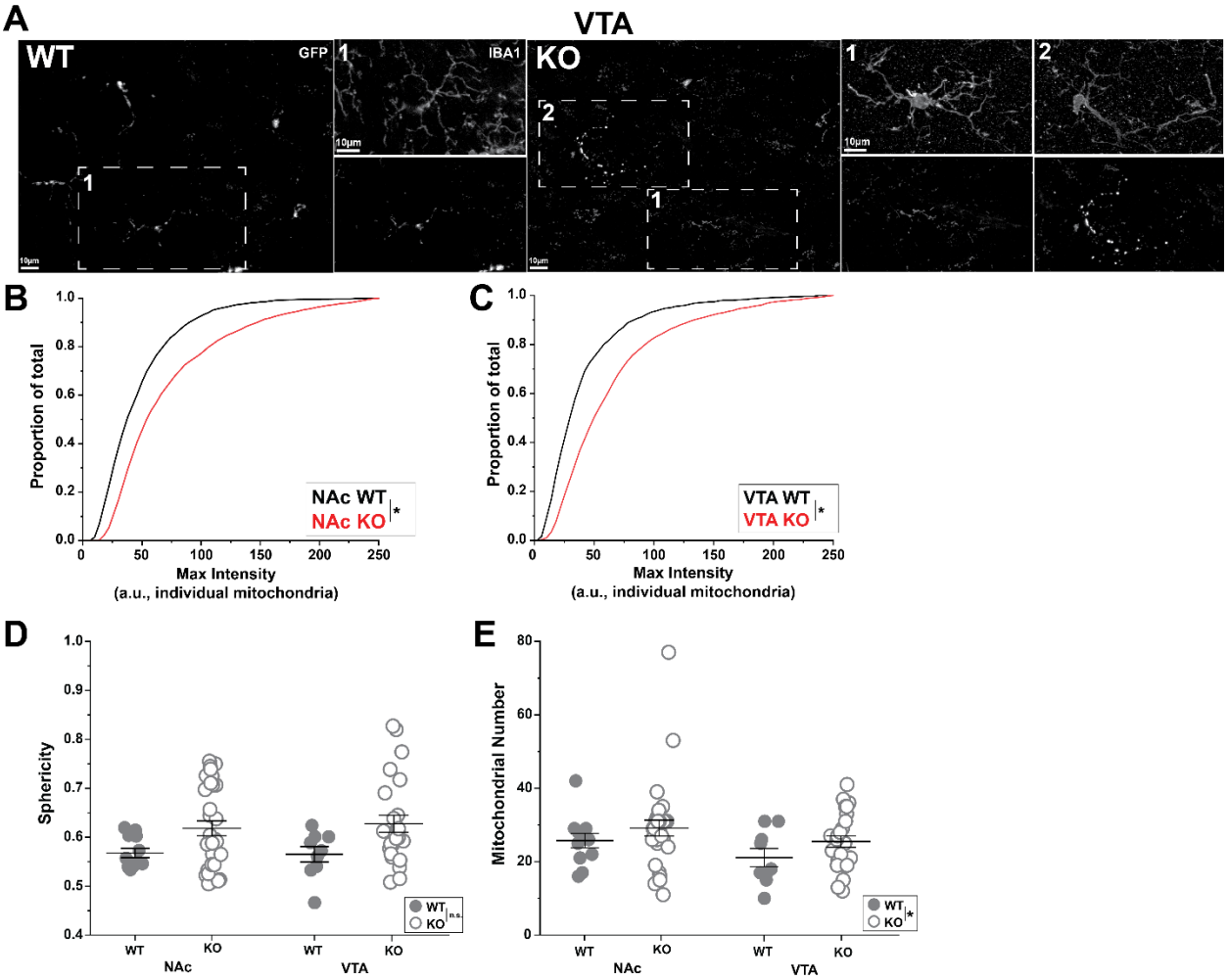

Figure S7: Mitochondria display altered morphology as a result of TFAM downregulation (continuation of Fig. 7) (A) Representative high-magnification images at 5 mos. of VTA microglia (Iba1) and mitochondria (GFP) in both WT control and TFAM KO mice. **(B-C)** Cumulative distribution of max intensity for individual mitochondria across FOV in both WT and TFAM KO mice in NAc and VTA. *B.* NAc WT = 2124 mitochondria KO=4063 mitochondria, Kolmogorov-Smirnov test p>0.0017 *C.*VTA WT=1468 mitochondria KO = 2684 mitochondria, Kolmogorov-Smirnov test p>0.0197. **(D)** Quantification of average sphericity of mitochondria across individual cells in NAc WT, KO and VTA WT, KO. Two-way Anova Genotype F = 2.4520 p = 0.1217, Region F = 2.8087 p = 0.0982. **(E)** Quantification of mitochondrial number across individual cells in NAc WT, KO and VTA WT, KO. Two-way Anova Genotype F = 8.1194 p = 0.0056, Region F = 0.0280 p = 0.8675 *D-E.* NAc WT N = 12 cells, KO = 31 cells and VTA WT = 9 cells, KO = 25 cells.

SUPPLEMENTARY FIGURE 8

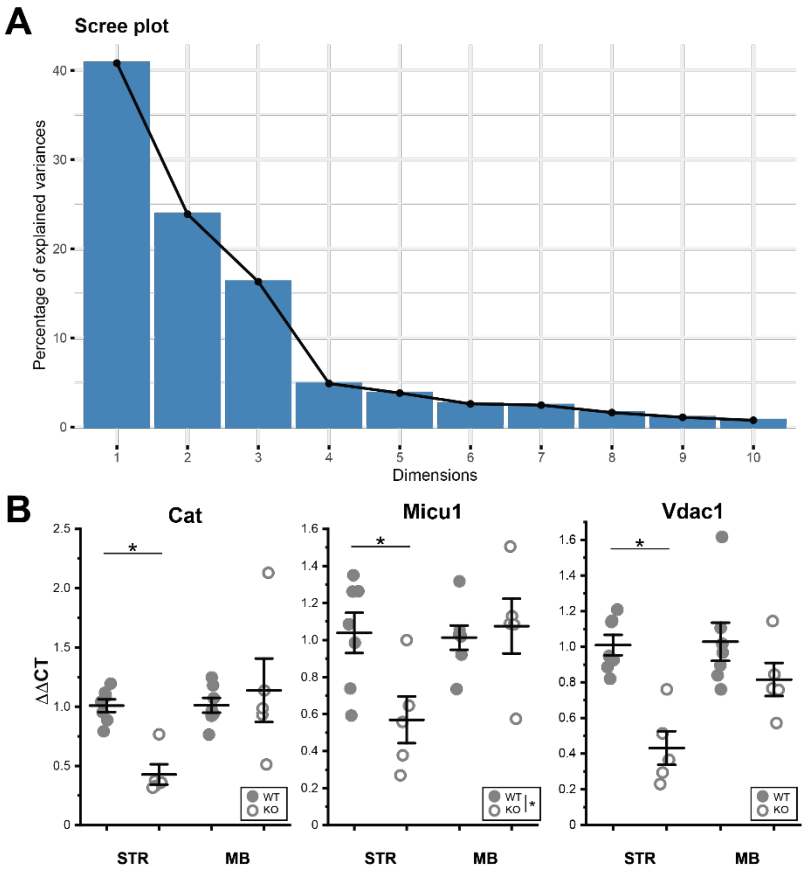

(A) Scree plot describing the percentage of explained variance for the Principal Component Analysis of control and MG-TFAMKO samples based on microglial- and mitochondrial- function related genes. **(B)** Quantification of normalized, relative expression (fold change or ΔΔCT) of mitochondrial function genes. See Table 5 for ANOVA and Post Hoc analysis values.

Supplementary Table 1: LPS Relative Gene Expression ANOVA Values.
Related to Figure 4B.

	Treatment		Region	
Gene	F Value	P Value	F Value	P Value
Tgfβ1	3.64818	0.03638	0.74976	0.39245
P2ry12	13.3998	0.0001	0.68065	0.41495
Csf1r	1.13966	0.34319	1.2454	0.27996
Cx3cr1	9.42003	0.000533	0.04288	0.83715
Cd68	4.11485	0.02483	5.06765	0.03076
Cd45	8.86009	0.00077	7.37401	0.01021
Itgam	14.09506	0.000246	1.07928	0.31341
Tnfα	10.23143	0.000317	0.01671	0.8979
Il1β	8.41188	0.00104	0.01627	0.89925
Micu1	5.40554	0.009	5.57555	0.02391
Cat	7.43629	0.00204	0.11711	0.73424
Ppargc1α	2.99706	0.06289	0.15601	0.69526
Nrf1	4.43215	0.01924	0.04594	0.83152
Mfn1	0.77771	0.46724	1.3191	0.25854
Dnm1l	4.8918	0.01338	0.31082	0.58072
Sod2	7.41671	0.00206	1.70341	0.20036
Tfam	2.1335	0.13357	1.72655	0.1974
Vdac1	12.4427	0.0001	0.06818	0.79554
Gpx1	20.79043	0.0001	1.01441	0.32076
Ndufa12	15.1893	0.0001	0.31724	0.57686
Atp5d	36.99749	0.0001	2.90216	0.09733
Cox4i1	12.11631	0.0001	1.69829	0.20102
Sdha	1.8012	0.18007	0.00647	0.93633

Supplementary Table 2: LPS Relative Gene Expression Post Hoc Analyses.
Related to Figure 4B.

Genes		LPS 4hr vs Saline	LPS 24hr vs Saline	LPS 24hr vs LPS 4hr	MB vs STR
Tgfβ1	Probability	0.29856	0.03572	1	0.41278
	T value	-1.69206	-2.65327	-0.91161	-0.8289
P2ry12	Probability	0.00101	0.0001	1	0.45099
	T value	-3.97331	-4.8306	-0.76698	-0.76229
Csf1r	Probability	0.56513	1	1	0.33355
	T value	-1.37044	-0.94236	0.46004	-0.99552
Cx3cr1	Probability	0.00041798	0.45199	0.02272	0.95445
	T value	-4.27642	-1.46937	2.83451	-0.05753
Cd68	Probability	0.17688	1	0.03203	0.03952
	T value	-1.95212	0.75952	2.69744	-2.13869
Cd45	Probability	1	0.00219	0.00309	0.00733
	T value	0.05282	3.7024	3.58036	2.84717
Itgam	Probability	0.2025	0.000191597	0.01835	0.25439
	T value	1.95288	5.25978	3.12856	1.17964
Tnfα	Probability	0.000198161	0.117796	0.03916	0.9941
	T value	4.52848	1.9492	-2.61572	-0.00745
Il1β	Probability	0.00078693	0.42024	0.04286	0.98861
	T value	4.06006	1.50976	-2.57852	-0.01438
Micu1	Probability	0.27588	0.00708	0.4393	0.02479
	T value	-1.73266	-3.27919	-1.48524	-2.34559
Cat	Probability	0.00198	0.04203	0.71437	0.82245
	T value	-3.73851	-2.58666	1.2002	-0.22609
Ppargc1α	Probability	0.16869	0.09614	1	0.71262
	T value	-1.97473	-2.23293	-0.21646	-0.37134
Nrf1	Probability	0.21664	0.78056	0.01577	0.89431
	T value	1.85378	-1.24449	-2.97688	0.13382
Mfn1	Probability	1	0.76394	1	0.23403
	T value	-0.95289	-1.15815	-0.18361	1.21095
Dnm1l	Probability	0.02817	0.03151	1	0.58201
	T value	2.7491	2.70405	-0.0956	0.55561
Sod2	Probability	0.02418	0.00246	1	0.21081
	T value	2.80989	3.6624	0.78404	1.2747
Tfam	Probability	0.14411	0.35257	1	0.20397
	T value	2.04883	1.6048	-0.47402	-1.2945
Vdac1	Probability	0.09993	0.027	0.0001	0.64942
	T value	-2.2157	2.76603	4.93002	0.4585
Gpx1	Probability	0.06221	0.000865327	0.0001	0.2331
	T value	-2.42235	4.02733	6.3744	1.2134
Nudfa12	Probability	1	0.0001	0.00026155	0.66075
	T value	0.4567	4.98498	4.43509	-0.44264
Atp5d	Probability	1	0.0001	0.0001	0.13839
	T value	-0.26036	7.3228	7.44627	-1.51645
Cox4i1	Probability	1	0.000437904	0.00068819	0.25917
	T value	0.065	4.26059	4.11594	-1.14698
Sdha	Probability	0.32009	1	0.38157	0.98235
	T value	-1.65582	-0.0952	1.5624	0.02229

Supplementary Table 3: LPS Microglila- and Mitochondrial- Function Gene Correlation Values. Related to Figure 4D.

		Cd45			Il1β			Tnfα		
Genes		Saline	LPS 4hr	LPS 24hr	Saline	LPS 4hr	LPS 24hr	Saline	LPS 4hr	LPS 24hr
Atp5d	p-value	0.243186	0.054409	0.422675	0.655035	0.261958	0.068148	0.453851	0.737764	0.07301
	R value	0.334	0.524	0.233	0.131	0.322	0.501	0.218	0.098	0.493
Cox4i1	p-value	0.115781	0.020008	0.008949	0.162115	0.343098	0.155616	0.112976	0.857977	0.295356
	R value	0.44	0.612	0.669	0.395	0.274	0.401	0.443	-0.053	0.301
Nudfa12	p-value	0.242291	0.00231	0.001688	0.718613	0.041942	0.050471	0.649297	0.147684	0.020906
	R value	0.335	0.743	0.758	0.106	0.549	0.531	0.133	0.408	0.609
Sdha	p-value	0.450617	0.000284	0.00158	0.658862	0.074233	0.875813	0.958116	0.301592	0.846165
	R value	0.22	0.825	0.761	0.13	0.492	0.046	0.015	0.298	0.057
Nrf1	p-value	0.259407	0.000842	0.003925	0.852717	0.008988	0.760069	0.69175	0.00567	0.832857
	R value	0.323	0.787	0.717	0.055	0.668	-0.09	0.116	0.696	-0.062
Tfam	p-value	0.874163	0.004251	0.006326	0.803208	0.005939	0.421008	0.499075	0.014526	0.603661
	R value	0.047	0.712	0.69	-0.073	0.694	0.234	-0.197	0.636	0.152
Ppargc1α	p-value	0.518132	0.007551	0.125748	0.219981	0.5074	0.309656	0.239796	0.563102	0.475501
	R value	-0.189	0.679	0.429	-0.35	0.194	0.293	-0.336	0.169	0.208
Dnm1l	p-value	0.255455	0.027207	1.86E-05	0.903408	0.001987	0.103279	0.573546	0.000308	0.023148
	R value	0.326	0.587	0.891	-0.036	0.75	0.454	0.165	0.822	0.601
Mfn1	p-value	0.298008	0.000239	0.000604	0.46486	0.006849	0.667476	0.703702	0.039963	0.565706
	R value	0.3	0.83	0.799	-0.213	0.685	0.126	0.112	0.554	0.168
Micu1	p-value	0.637384	0.006495	0.200337	0.183293	0.099527	0.223598	0.829954	0.623895	0.110662
	R value	0.138	0.688	0.364	0.378	0.458	-0.347	0.063	0.144	-0.445
Vdac1	p-value	0.132387	0.006258	0.026315	0.768373	0.722023	0.17943	0.202406	0.408627	0.236248
	R value	0.422	0.691	0.59	0.087	0.105	0.381	0.363	-0.24	0.339
Sod2	p-value	0.095783	0.656759	0.791282	0.332263	0.00051	0.049946	0.093852	0.00047	0.008993
	R value	0.463	0.13	0.078	0.28	0.805	0.533	0.465	0.808	0.668
Cat	p-value	0.017759	0.068415	0.15402	0.112545	0.31547	0.273258	0.074569	0.050841	0.146902
	R value	0.621	0.5	0.402	0.443	-0.289	-0.315	0.491	-0.531	-0.409
Gpx1	p-value	0.040339	0.116319	0.000114	0.070438	0.147068	0.307691	0.290397	0.104706	0.180963
	R value	0.553	0.439	0.851	0.497	-0.408	0.294	0.304	-0.452	0.379

		Cx3cr1			P2ry12			Tgfβ1		
Genes		Saline	LPS 4hr	LPS 24hr	Saline	LPS 4hr	LPS 24hr	Saline	LPS 4hr	LPS 24hr
Atp5d	p-value	0.410507	0.507675	0.934088	0.476733	0.513171	0.115752	0.18298	0.017449	0.43138
	R value	0.239	0.193	0.024	0.207	0.191	-0.44	0.378	0.622	-0.229
Cox4i1	p-value	0.002718	0.059727	0.001538	0.04562	0.047682	0.564532	0.000121	0.01133	0.129875
	R value	0.736	0.515	0.762	0.541	0.537	0.169	0.849	0.653	0.425
Nudfa12	p-value	0.008378	0.623349	0.076011	0.006493	0.366739	0.371298	0.006554	0.002106	0.869059
	R value	0.673	0.144	0.489	0.688	0.261	-0.259	0.688	0.748	0.049
Sdha	p-value	0.004549	0.382336	0.000201	0.000489	0.250465	0.06339	0.005378	0.010413	0.00232
	R value	0.709	0.253	0.835	0.807	0.329	0.508	0.699	0.659	0.743
Nrf1	p-value	0.026509	0.616306	7.19E-05	0.00873	0.816145	0.046178	0.011859	0.021657	0.008035
	R value	0.59	-0.147	0.863	0.67	-0.068	0.54	0.65	0.606	0.675
Tfam	p-value	0.156288	0.530575	2.73E-06	0.018423	0.767284	0.103588	0.133879	0.013729	0.007085
	R value	0.4	-0.183	0.922	0.618	-0.087	0.453	0.421	0.64	0.683
Ppargc1α	p-value	0.305367	0.331094	0.031964	0.037368	0.171057	0.151528	0.376428	0.048401	0.054397
	R value	0.295	0.281	0.574	0.56	0.387	0.404	0.256	0.536	0.524
Dnm1l	p-value	0.115107	0.075744	0.035223	0.129566	0.169954	0.666568	0.16688	0.09772	0.664119
	R value	0.44	-0.489	0.565	0.425	-0.388	-0.126	0.391	0.46	0.127
Mfn1	p-value	0.246613	0.779622	6.76E-05	0.26496	0.973076	0.093375	0.374466	0.025203	0.012711
	R value	0.332	-0.082	0.864	0.32	-0.01	0.466	0.257	0.594	0.645
Micu1	p-value	0.006706	0.152296	0.000361	0.002054	0.093731	4.12E-05	0.002998	0.00414	9.65E-05
	R value	0.686	0.404	0.817	0.749	0.465	0.875	0.731	0.714	0.855
Vdac1	p-value	0.818976	0.020545	0.137403	0.975162	0.021355	0.85242	0.427631	0.044513	0.503071
	R value	0.067	0.61	0.418	0.009	0.607	0.055	0.231	0.544	0.195
Sod2	p-value	0.228609	0.030824	0.139799	0.410051	0.049988	0.029747	0.047076	0.216666	0.057862
	R value	0.344	-0.577	-0.415	0.239	-0.532	-0.58	0.538	0.352	-0.518
Cat	p-value	0.026453	8.66E-07	5.16E-05	0.084368	1.86E-06	8.73E-06	0.002832	0.078165	2.00E-06
	R value	0.59	0.936	0.87	0.477	0.927	0.905	0.733	0.486	0.926
Gpx1	p-value	0.002105	0.000371	0.006925	0.04628	0.00011	0.995596	0.00704	0.157777	0.272069
	R value	0.748	0.816	0.684	0.54	0.852	-0.002	0.683	0.399	0.315

Supplementary Table 4: LPS CD68 and Mitochondrial Function Gene Correlation Values. Related to Figure S4.

		Cd68		
Genes		Saline	LPS 4hr	LPS 24hr
Atp5d	p-value	0.244953	0.072956	0.597781
	R value	0.333	0.493	0.155
Cox4i1	p-value	0.022299	0.001642	0.005179
	R value	0.604	0.759	0.701
Nudfa12	p-value	0.044364	0.002696	0.009273
	R value	0.544	0.736	0.666
Sdha	p-value	0.000925	0.003644	0.002434
	R value	0.783	0.721	0.741
Nrf1	p-value	0.041921	0.147633	0.000147
	R value	0.549	0.408	0.844
Tfam	p-value	0.142168	0.082639	2.80E-05
	R value	0.413	0.48	0.883
Ppargc1α	p-value	0.168117	0.011502	0.01246
	R value	0.39	0.652	0.647
Dnm1l	p-value	0.16642	0.521566	0.038072
	R value	0.391	0.187	0.558
Mfn1	p-value	0.426371	0.12996	0.001682
	R value	0.231	0.425	0.758
Micu1	p-value	4.48E-05	0.002633	0.013571
	R value	0.873	0.737	0.641
Vdac1	p-value	0.717459	0.003202	0.437407
	R value	0.106	0.727	0.226
Sod2	p-value	0.245894	0.313307	0.101732
	R value	0.332	-0.291	-0.455
Cat	p-value	0.031319	0.001214	0.007711
	R value	0.575	0.772	0.678
Gpx1	p-value	0.023396	0.002231	0.017928
	R value	0.6	0.745	0.62
Il1β	p-value	0.285311	0.743132	0.633467
	R value	0.307	-0.096	0.14
Tnfα	p-value	0.890133	0.573917	0.779166
	R value	-0.041	-0.165	0.083
Tgfβ1	p-value	8.64E-05	0.01461	0.009268
	R value	0.858	0.635	0.666
Cd45	p-value	0.814098	0.083225	0.01459
	R value	0.069	0.479	0.635
Cx3cr1	p-value	4.05E-05	0.009317	2.61E-05
	R value	0.876	0.666	0.885
P2ry12	p-value	3.48E-05	0.001087	0.157866
	R value	0.879	0.777	0.399

Supplementary Table 5: MG-TFAMKO Normalized Relative Gene Expression (ΔΔCT) ANOVA Values. Related to Figure 8 and Figure S5.

	ANOVA - Genotype		ANOVA - Region		TFAMKO STR vs WT STR		TFAMKO MB vs WT MB	
Genes	F Value	P Value	F Value	P Value	T Value	Probability	T Value	Probability
Atp5d	**8.24152**	**0.00945**	**9.08104**	**0.00686**	-0.08877	1	**4.1487**	**0.00298**
Cat	3.2315	0.08735	**7.95272**	**0.01058**	**-3.24837**	**0.02415**	0.70613	1
Cd45	**9.34874**	**0.00621**	4.1495	0.0551	**-3.7018**	**0.00847**	-0.62226	1
Cd68	**40.90433**	**0.0001**	**8.83476**	**0.00753**	**-6.58093**	**0.0001**	-2.46388	0.13759
Cox4i1	**77.13244**	**0.0001**	**36.30092**	**0.0001**	2.02807	0.3365	10.39228	**0.0001**
Cx3cr1	**15.18122**	**0.0008965**	3.98099	0.05982	**-4.1624**	**0.00289**	-1.34781	1
Gpx1	1.85696	0.18812	2.23482	0.15054	-2.0151	0.3452	0.08795	1
Il1β	**5.18021**	**0.03399**	3.82433	0.06463	0.2358	1	**2.98296**	**0.04411**
Micu1	3.38639	0.08063	**4.70818**	**0.04224**	**-3.00055**	**0.0424**	0.15657	1
Ndufa12	0.64297	0.43206	2.74313	0.11328	-0.54693	1	1.68092	0.64998
Sdha	**5.14226**	**0.03458**	2.08093	0.16463	-2.65204	0.09179	-0.5549	1
Sod2	**5.24894**	**0.03295**	**7.49207**	**0.0127**	**-3.46467**	**0.01468**	0.22463	1
Tfam	**115.41048**	**0.0001**	1.65424	0.21307	**-8.58753**	**0.0001**	**-6.60527**	**0.0001**
Tgfβ1	**15.1938**	**0.000893**	2.92247	0.10283	**-3.92324**	**0.00505**	-1.58926	0.76612
Tnfα	**14.76834**	**0.00102**	2.32982	0.14258	1.54353	0.83026	**3.89123**	**0.00544**
Vdac1	**18.76714**	**0.0003237**	**4.88124**	**0.03898**	**-4.48229**	**0.00137**	-1.64423	0.69454

Supplementary Table 6: Primers and probes used for qPCR experiments. Related to Figures 4 and S4.

Gene	TaqMan Assay ID or custom probe	Forward Primer	Reverse Primer
Aldh1l1	Mm03048957_m1		
Atp5d	Mm00502864_m1		
Cat	Mm00437992_m1		
Cd45 (Ptprc)	Mm01293577_m1		
Cd68	Mm03047343_m1		
Cox4i1	Mm01250094_m1		
Csrf1	Mm01266652_m1		
Cx3cr1	Mm00438354_m1		
Dnm1l	Mm01342903_m1		
Gapdh	MGB - CTCATGACCACAGTCCA - VIC	GACAACTTTGGCATTGTGGAA	CACAGTCTTCTGGGTGGCAGTGA
Gpx1	Mm04207457_g1		
Il1β	Mm00434228_m1		
Itgam	Mm00434455_m1		
Mfn1	Mm00612599_m1		
Micu1	Mm00522783_m1		
Nrf1	Mm01135606_m1		
Nudfa12	Mm01240336_m1		
Olig1	Mm00497537_s1		
Olig2	Mm01210556_m1		
P2ry12	Mm00446026_m1		
Ppargc1α	Mm01208835_m1		
Ppp1r1b	Mm00454892_m1		
Sdha	Mm01352366_m1		
Slc1a2	Mm01275814_m1		
Slc32a1	Mm00494138_m1		
Sod2	Mm01313000_m1		
Tfam	Mm01148667_m1		
Tgfβ1	Mm01178820_m1		
Tnfα	Mm00443258_m1		
Vdac1	Mm00834272_m1		